AIAA 2003-0591

Transonic Experimental Observations of Abrupt Wing Stall On an F/A-18E Model (Invited)

S. Naomi McMillin, Robert M. Hall, and John E. Lamar
NASA Langley Research Center
Hampton, VA

41st Aerospace Sciences Meeting and Exhibit
6 – 9 January 2003
Reno, Nevada

Transonic Experimental Observations of Abrupt Wing Stall On an F/A-18E Model

S. Naomi McMillin*, Robert M. Hall†, and John E. Lamar†
NASA Langley Research Center
Hampton, Virginia

ABSTRACT

A transonic wind tunnel test of an 8% F/A-18E model was conducted in the NASA Langley Research Center (LaRC) 16 ft Transonic Tunnel (16-ft TT) to investigate on-surface flow physics during stall. The technical approach employed focused on correlating static (or time-averaged) and unsteady wind-tunnel test data to the unsteady wing-stall events using force, moment, pressure, and pressure-sensitive-paint measurements. This paper focuses on data obtained on the pre-production configuration of the F/A-18E aircraft at Mach number of 0.90. The flow unsteadiness occurring on the wing as the wing went through the stall process was captured using the time history of balance and pressure measurements and by calculating the root mean square (RMS) for a number of instrument signals. The second step was to gather global perspectives on the pressures influencing the wing stall process. The abrupt wing stall experienced by the 8% F/A-18E Model was observed to be an unsteady event triggered by the rapid advancement of separation, which had migrated forward from the trailing edge, to the leading-edge flap hingeline over a very small increment in angle of attack. The angle of attack at which this stall occurred varied, from run to run, over an 1° increment. The abrupt wing stall was observed, using pressure-sensitive-paint, to occur simultaneously on both wing panels or asymmetrically. The pressure-sensitive paint data and wing-root bending moment data were essential in providing insight to the flow structures occurring over the wing and the possible asymmetry of those flow structures. A repeatability analysis conducted on eight runs of static data provided a quick and inexpensive examination of the unsteady aerodynamic characteristics of abrupt wing stall. The results of the repeatability analysis agreed extremely well with data obtained using unsteady measurement techniques. This approach could be used to identify test conditions for more complex unsteady data measurements using special instrumentation.

INTRODUCTION

The Abrupt Wing Stall (AWS) Program has been an applied aerodynamics effort addressing uncommanded lateral motions, a challenge that has plagued a significant number of aircraft over at least the last 50 years. The impetus of this program was the wing drop encountered during the Engineering, Manufacturing, and Development (EMD) phase of the F/A-18E/F Program, see reference 1. Figure 1 shows a picture of the F/A-18E/F aircraft. After significant expenditure of flight test and analysis resources, the lateral activity was mitigated by very costly flight-derived fixes for the F/A-18E/F and the aircraft proceeded into production phase. However, the fact remains that the lateral instability was not predicted prior to flight testing. Consequently, a cooperative NASA/Navy/Air Force program was charged with developing methods and procedures to analyze and predict uncommanded motions for future aircraft.

A key component of this research was a series of wind-tunnel test programs to investigate the abrupt wing stall phenomenon and develop a strategy for future testing and analysis of aircraft susceptible to abrupt wing stall. The program had the advantage of access to several databases from the F/A-18E/F developmental program including transonic wind-tunnel force and moment data and oil flow visualization, Navier-Stokes computations, and flight-test data. Based on a study of these databases, an experimental strategy was developed to fill in the flow understanding "gaps" surrounding the abrupt wing stall phenomena as exhibited by an F/A-18E model (preproduction configuration). The technical approach employed focused on correlating static (or time-averaged) and unsteady wind-tunnel test data to the unsteady wing-stall events using force, moment, pressure, and pressure-sensitive-paint measurements.

* Aerospace Engineer, Configuration Aerodynamics Branch

† Aerospace Engineer, Configuration Aerodynamics Branch, Associate Fellow, AIAA

This paper describes the wind-tunnel model, instrumentation, data acquisition techniques, analysis results, and the interpretation of the data as it relates to an improved understanding of the abrupt wing stall phenomenon as it occurred on the preproduction baseline configuration using the 8% F/A-18E Model. In order to obtain approval for releasing this paper to the public, quantitative information has been removed from most vertical scales as per guidelines from the Department of Defense.

SYMBOLS AND ABBREVIATIONS

16-ft TT – NASA Langley Research Center 16 Foot Transonic Tunnel

AWS - abrupt wing stall

BL – semi-span station measured from aircraft centerline, full scale length, in.

c – local wing chord

C_A – axial force coefficient

C_D – drag force coefficient

C_l – rolling moment coefficient

C_L – lift force coefficient

C_m - pitching moment coefficient

C_n - yawing moment coefficient

C_N - normal force coefficient

C_p - wing surface pressure coefficient

C_{WM} - wing-root bending-moment coefficient

C_y - side force coefficient

EMD – Engineering and Manufacturing Development

ESP - electronic pressure scanning

M - free-stream Mach number

PSP - pressure sensitive paint

RMS - root mean squared

x - distance on wing planform from the wing leading edge, inches

α - angle of attack, degrees

α_{st} - angle of attack where the C_L vs. α curve had a significant break in slope

β - sideslip angle, degrees

TECHNICAL APPROACH

A two-step approach was used in the correlation of static wind-tunnel data and unsteady wing stall occurring on an 8% model of the pre-production F/A-18E/F aircraft. The first step in this technical approach was to capture the unsteadiness occurring on the wing as the wing went through the stall process. The second step was to gather global perspectives on the pressures influencing the wing stall process. In carrying out these steps, several experimental techniques were employed in two test entries in the Langley 16-ft. Transonic Tunnel (16-ft TT).

Model and Instrumentation Description

The 8% F/A-18E Model was modified to accommodate six sets of instruments. The instrumentation included the following types: static, unsteady, and optical.

Model Description

The model tested in the Langley 16-ft TT was an 8% model of the preproduction F/A-18E configuration. This particular model was the test article in the F/A-18E/F program for the development of this aircraft, and had been used previously for tests in the Veridian 8-ft. transonic tunnel. The model was originally designed to hold a six-component internal balance and steady pressure ports on the fuselage and ducts. The model was modular in nature, such that the wings, ducts, and tails could be removed and replaced with different geometries. This modularity allowed two new wing spars and flaps to be fabricated and used on the existing fuselage. The new wings had the identical geometry as the pre-production wing geometry of the F/A-18E. The wing did not include the porous wing fold fairing arrangement of the production aircraft. Rather, the fold fairing door was solid for the current investigation.

This paper deals solely with the pre-production baseline leading-edge and trailing-edge geometry tested in the F/A-18E/F development program with a 10°/10°/5° flap set where the deflection notation corresponds to the leading-edge flap deflection, the trailing-edge flap deflection, and the aileron deflection, respectively. This configuration is referred to hereafter as the baseline configuration. This flap set is representative of the 6.1.3 version of the flight control laws developed as the "80% solution" to the abrupt wing stall problem as it occurred in the aircraft development program.

Instrumentation

Six sets of instrumentation were used in the test program: 1) an internal six-component strain-gage

balance, 2) three internal 64-port electronic pressure scanning (ESP) modules for sampling 168 wing steady pressure ports, 3) 22 unsteady wing pressure transducers, 4) four outer-wing accelerometers, 5) two wing-root bending-moment strain gages, and 6) a pressure-sensitive-paint flow visualization system.

Three wing panels were fabricated. Two versions of the wing panel were used. The first left wing panel, referred to as the heavily instrumented wing panel, was instrumented to obtain unsteady data simultaneously with static data on the surface of the wing. This panel, shown in figure 2(a), contained steady pressure ports, in-situ unsteady pressure transducers, outer-wing accelerometers, and wing-root bending-moment gauges. The majority of pressure ports were located on the upper surface of the wing.

Due to instrumentation complexity and cost, the right wing panel had no unsteady wing pressure transducers and a reduced number of steady pressure ports as shown in figure 2(b). The third wing panel, a left wing panel which mirrored the reduced instrumentation of the right wing, was fabricated for obtaining pressure-sensitive-paint data simultaneously with static data. Thus, unsteady pressure ports were not included on this left wing panel or the right wing panel, since the instrumentation would not survive the harsh chemicals used to apply and remove the coats of pressure sensitive paint. Figures 2(b) and 2(c) show the instrumentation for the instrumented right wing and the lightly instrumented left wing.

Experimental Approach

The first step in the technical approach was to capture the unsteadiness occurring on the wing as it went through the stall process. This step was accomplished using three data acquisition techniques: repeat runs, root-mean-squared (RMS) signals, and time histories. The second step was to gather global looks at the pressures influencing the wing stall process. This step was accomplished using the pressure-sensitive-paint (PSP) technique, with its advantage of providing continuous pressure information across the span, rather than at the discrete spanwise locations associated with pressure ports.

Tunnel and Flow Conditions

The model was tested in the 16-ft TT at NASA Langley Research Center. Figure 3 shows the model installed in tunnel test section. The 16-ft TT is a single-return, continuous-flow, atmospheric tunnel with air exchange and a slotted octagonal test section. A complete description of this wind tunnel and its operating characteristics is presented in reference 2. Testing was performed at atmospheric conditions for $0.5 \leq M \leq 0.9$. Data were obtained over the angle of attack (α) range of -4° to 16° and over the sideslip angle (β) range of –5° to 5°. The intention of this paper is to limit the data review to those factors that define the flow phenomena associated with the abrupt wing stall issue. Thus, this paper discusses only data obtained over the α-range on the pre-production baseline F/A-18E geometry with a 10°/10°/5° flap setting at $M = 0.9$ and $\beta = 0°$.

When the model was tested at wing stall conditions, the model visibly exhibited significant dynamic motions, which were combinations of pitch, plunge, and roll. The intensity of the dynamic motions varied from run to run for the same configuration. Repeat runs would often have different intensity levels in dynamic motions. The testing procedure included monitoring the balance for proximity to the balance force and moment limits. During the α-range associated with abrupt wing stall, it was not uncommon for the balance limits to be exceeded. When this occurred, the model angle of attack was quickly increased and the motions subsided, or Mach number was quickly decreased. It should be noted that the model exhibited this vibration whether the model approached the critical α-range from lower or higher angles of attack.

Static Data

To further understand and correlate with the unsteadiness of the stall process, time-averaged data were obtained to understand the flow structure over the wing before the stall occurred. The static data obtained were configuration force/moment data, wing surface pressure data, and wing-root bending-moment data. The static data were obtained using the data acquisition system of the 16-ft TT. The signals from the various equipment were passed through a low-pass filter (1 Hz) and then sampled for 5 seconds at a 10 sample/second rate. The average of the samples was then used as static data (also referred to as time-averaged data).

Repeat Runs

Since previous testing showed that the model would vibrate on the sting/strut assembly in the tunnel at wing-drop conditions, it was necessary to determine the repeatability of the static data in this α-range. A series of repeat runs was therefore conducted in each test entry. The repeat runs were conducted on the baseline configuration at $M = 0.9$. The baseline configuration was installed at the beginning, middle, and end of a test entry. Several back-to-back runs were obtained for each baseline configuration installation. A simple statistical analysis was conducted on the set of repeat runs for each

test entry. As discussed in a later section, data from the repeatability analysis were found to correspond extremely well with other markers of the flow unsteadiness.

RMS Measurements

Another effort made to capture the character of the flow unsteadiness involved in routing the signals from the balance, unsteady pressure transducers, wing strain gages, and outer-wing accelerometers through RMS (root mean square) boards that calculated running values of RMS for the respective signals. This value of the RMS was then recorded by the usual time-filtered tunnel data acquisition system. These RMS signals do not, of course, contain any information as to the frequency or character of the true time history.

Time History Measurements

The second, more resource intensive, level of unsteadiness measurement was to record the time histories of various parameters. The dynamic data acquisition system employed in this effort was capable of acquiring time-synchronized data on 32 channels. Three balance channels, 23 unsteady pressure transducers, 2 wing-root bending-moment gages, and the 4 outer-wing accelerometers were dynamically sampled. The 3 balance channels chosen for dynamic sampling were the axial-force, pitching-moment, and rolling-moment components.

During the test, the unsteady data were acquired in 10-second records on magnetic tape using VHS videocassettes and digitized post-test. In the digitizing process, the data were sampled at a rate of 1000 samples per second for 10 seconds. A 200 Hz anti-aliasing filter was applied to data during the digitization process. Time history records, mean, standard deviation, and maximum and minimum values were processed for each data point and channel in the data set. The data were stored on a compact disk volume for further data processing by the AWS team. Initial data analysis from this data set is discussed in reference 3.

Pressure Sensitive Paint Measurements

The second entry of the model focused on gathering global looks at the pressures influencing the wing stall process through the use of the PSP technique. Figure 4 shows photographs of the model with a coating of PSP on the upper surface of the wings as installed in the 16-ft TT. Reference 4 contains a more detailed description of the PSP testing technique. The discussion here will cover some details that significantly influenced the testing.

Before a PSP coating could be applied, the surface of the model had to be at room temperature. This limitation required extensive down time between configuration changes, since the model would heat up significantly during a test run. Once the PSP coat was applied and dry, the registration marks could be applied and measured. Overall, the time consumed in the application process is a limiting factor in the use of this technique in the wind-tunnel testing environment.

Another time-consuming task in the PSP process was the necessity to take wind-off images after each wind-on run. This step took longer than the actual wind-on run because the wind-off images were acquired at finer angle-of-attack increments than those taken in the actual wind-on run. This step was necessary to find a suitable wind-off image corresponding to each wind-on image in the calibration process.

Figures 2b and 2c show locations of the measured pressure ports used to calibrate the PSP images. The PSP coat was applied to the surface of the wing aft of the trip dots, as shown in figures 4(b) and 4(c). Therefore, the first pressure port in each row was not used in the calibration. Other ports were eliminated on a case-by-case basis due to bad pressure port data, extreme pressure gradients occurring directly over the port, or inability of the calibration algorithm to accommodate that specific pressure data. Figures 5 and 6 show a comparison of the measured pressures from the static pressure data (referred to hereafter as ESP data) with pressures resulting from the PSP data reduction algorithm at the ports used for the calibration. Figure 5 shows the comparisons for α = 8.0° and figure 6 shows the comparison at α = 10.0°. All data presented in this paper will be for M = 0.90. Recall that a static measurement is an average of 50 samples of data acquired over a 5 second time period. In contrast, the PSP photographic image is acquired over a much shorter time period of 1.5 seconds. The acquisition of both the ESP and PSP data begins at the same time. The comparison of ESP measured and PSP calibrated data is remarkably good even in the α-range of abrupt stall (see figure 6).

The upper surface of the wing was fabricated with trenches, which contained the pressure tubing and wiring. The trenches were filled in with body fill material. Since this fill material has different thermal characteristics than the steel of the model, the PSP results were affected slightly over these areas. Although the PSP post-processing was able to eliminate much of this effect, some shadows of the trenches remain in the PSP images, as seen in figure 7.

Figure 8 compares a PSP image with an oil flow obtained in a previous entry of this model with the original uninstrumented wings in the Veridian tunnel. Both sets of data are for the baseline configuration at $M = 0.9$ and $\alpha = 8.0°$. The flow features are captured by both techniques as identified in the figure. The PSP technique can capture more angles of attack in a given run than the oil flow technique.

The post-processing of the PSP images is time intensive and not automatic. One feature of the process is assigning color to pressure values. A color bar is generated which assigns a maximum and minimum value to the extremes of the color bar. For the sake of comparison in this paper, all of the PSP images used the same color bar, even though the maximum and minimum values of each image were different.

ANALYSIS OF ABRUPT WING STALL

Over 500 data runs were obtained from the two test entries of the 8% F/A-18E model in the 16-ft TT. These data define the effects of test conditions and variations of the model in detail. Discussion of the full data set is beyond the intended scope of this paper. The following discussion is limited to the baseline configuration at $M = 0.9$, $\beta = 0°$ and over an angle-of-attack range of -2° to 14°.

Static Data and Pressure Sensitive Paint Data

Figure 9(a) shows the lift, rolling moment, and wing-root bending-moment coefficient data (C_L, C_l, and C_{WM}, respectively) for the baseline configuration at $M = 0.9$ over an angle-of-attack range of -2° to 14°. The drag, side-force, pitching-moment, and yawing-moment coefficient data (C_D, C_y, C_m, and C_n, respectively) are presented in figure 10 for completeness. However, the discussion here will focus on C_L, C_l, and C_{WM}. Figure 9(b) shows a closeup of these three coefficients in the angle of attack range where abrupt wing stall occurred. The angle of attack at which wing stall occurs, α_{st}, is defined as the angle of attack where the C_L vs. α curve had a significant break in slope. The C_L data of figure 9 show that for Run 1334 $\alpha_{st} = 9.1°$. The left and right C_{WM} data indicate that the wing stall is not symmetrical. The right wing panel stalls before the left wing panel at $\alpha = 9.1°$. The net result at this angle of attack is a slightly positive configuration rolling moment coefficient. However, the rolling moment varies with α, as indicated by the changing sign of C_l. At $\alpha = 10.6°$, the left wing panel has also stalled such that the left wing panel has less lift and a negative C_l was measured.

The above observations are supported by the wing surface coefficient (C_p) data as shown for representative angles of attack in figure 11. At $\alpha = 8.0°$ (figure 11a), the pressure distributions for all 5 rows are symmetrical between the left and right wing panels. However, at $\alpha = 9.1°$ (figure 11b), the right wing has a higher pressure (and thus less suction) near the center of the wing chord and across the span, indicating a loss in lift on the right wing and thus a positive rolling moment. At $\alpha = 10.6°$ (figure 11d), the left wing has the higher pressure, indicating a loss in lift on the left wing (compared to the right wing) and thus a negative rolling moment.

Figure 12 shows PSP data for this run at $\alpha =$ 6.1°, 7.1°, 8.0°, 8.6°, 9.1°, 9.6°, 10.0°, 10.6°, and 11.1°. The PSP data of figure 12 show several flow features identified in figure 8. However, for relevance to the abrupt wing stall phenomenon, the migration of separation from the trailing-edge to the leading-edge flap is the flow feature to be discussed here. At the lower angles of attack, $\alpha \leq 8.6°$, the PSP data clearly show separation at the mid-span of the wing advancing from the trailing-edge hingeline towards the leading-edge with increasing α. This separation is fairly symmetrical between the right and left wings from $6.1° \leq \alpha \leq 8.6°$. At $\alpha = 9.1°$, the trailing-edge separation on the right wing suddenly advanced all the way to the leading-edge flap hingeline just inboard of the leading-edge snag. The separation on the left wing moved forward from its position at $\alpha = 8.6°$ but did not appear to reach the hingeline at $\alpha = 9.1°$ nor at $\alpha = 9.6°$. At $\alpha = 10.0°$, the PSP data show that the separation reached the leading-edge flap hingeline for both wings.

Recall, that the C_{WM} and C_l data of figure 9 and the C_p data of figure 11 showed that, at $\alpha = 10.5°$, the left wing had less lift (indicated by a lower C_{WM} and greater pressure than was observed on the right wing). The result was a negative rolling moment for the configuration. While the PSP data do not show any asymmetry in the extent of flow separation features between the left and right wing, the PSP data do show higher values of C_p behind the separation front on the left wing compared to the right wing. This observation corresponds to ESP data of rows I and J on the left and right wings at $\alpha = 10.5°$ (see figure 11d). Consequently, there is very good agreement between the PSP images, the ESP pressure data, wing-root bending-moment gage data, and model balance data.

Repeatability Analysis and Pressure Sensitive Paint Data

As discussed in the *Tunnel and Flow Conditions* section, the model would vibrate in a pitch/plunge

motion when the model was moved into the critical range near $\alpha = 9°$. This vibration can be interpreted as an indicator of the abrupt wing stall occurring on the wing and illustrates the unsteady nature of the stall process.

Another measure of the unsteadiness of the flow phenomena can be found in a repeatability analysis of the data from the test. During the wind-tunnel entry for the PSP data runs, the baseline configuration was tested for a total of 8 runs. These runs are grouped into 4 sets where a set is defined as a particular installation of flaps and a coating of PSP. These four data sets are referred to hereafter as the baseline data set. Table 1 shows the model changes and PSP changes that occurred between the four sets of data.

Table 1. Model and PSP Changes In Between Sets of Baseline Data

Sets	Model Work Done
1 and 2	5 flap configurations and 4 PSP coatings applied
2 and 3	Removal and reinstallation of sting/balance/model assembly, PSP coating applied
3 and 4	2 flap changes and a new PSP coating applied

Figure 13 shows the balance force/moment coefficient and wing-root bending-moment coefficient data for all 8 runs. A simple statistical analysis was used to determine the mean (or average) and the standard deviation (σ), at each angle of attack, for the eight runs of data. Figure 13 also shows the averaged data from the baseline data set. The shaded area in figure 13 represents the extent of uncertainty in the data, based on a 2σ band around the average of the data. Thus, the 2σ band represents where one would expect 95% of collected data to reside. The standard deviation of all of the coefficients (except C_D and C_n) significantly in-creases over a 1.5° range of α, $9° < \alpha < 10.5°$. As discussed earlier, the model/sting assembly was observed to have a pitch/plunge behavior at this α-range and the intensity of this behavior would vary run to run. In fact, data were not obtained at $\alpha = 10.5°$ for the Set 2 runs because the model dynamics generated unacceptable balance loads preventing a pause at that condition. However, for all of the other runs data were obtained in this α-range as the balance loads remained acceptable despite any unsteady pitch/plunge motion of the model/sting assembly.

One reason for this increase in data scatter is that each run of the baseline data set experienced wing stall at a slightly different angle of attack as marked in Figure 13(a). Another reason for the data scatter could be the unsteady pitch/plunge behavior of the model at this angle of attack. The behavior of the model varied run to run discussed earlier. Table 2 lists α_{st} for each data set.

Table 2. Angle of Attack of Abrupt Wing Stall for Each Data Set

Data Set	α_{st}
1 (Runs 1199 and 1205)	9.9
2 (Runs 1289 and 1290)	9.4
3 (Runs 1291 and 1292)	9.0
4 (Runs 1332 and 1334)	9.1

Figure 13(a) and Table 2 show that α_{st} can vary with run and will occur at $9° \leq \alpha \leq 9.9°$. The PSP data also substantiate that wing stall occurred at different angles of attack for different runs. Recall that the PSP data for Run 1334 (see figure 12) showed that at $\alpha_{st} = 9.1°$ the separation at the mid-span location on the right wing had advanced to the leading-edge flap hingeline. The PSP data for Run 1199 from Set 1 and Run 1334 from Set 3 show similar results. Figures 14 and 15 show PSP data for Run 1199 and Run 1291, respectively, for $8° < \alpha < 11°$. The PSP data of figure 14 show the separation for both wing panels as being aft of the leading-edge flap hingeline for $\alpha \leq 9.4°$. At $\alpha_{st} = 9.9°$, for Run 1199, the separation has advanced to the leading-edge flap hingeline. Likewise, for Run 1291, the PSP data of figure 15 show the separation for both wing panels as being aft of the leading-edge flap hingeline for $\alpha \leq 8.6°$. At $\alpha_{st} = 9.0°$, for Run 1291, the separation on the left wing panel has advanced to the leading-edge flap hingeline.

Not only did α_{st} vary for different runs, but also the symmetry of the wing stall as recorded in Table 3. The data of Table 3 was obtained by using the PSP data of figures 12, 14, and 15 to determine the value of α at which the separation, migrating from the trailing-edge at the mid-span, reached the leading-edge flap hingeline.

Table 3. Angle of Attack Where Separation Has Reached the Leading-edge Flap Hingeline

	Right Wing Panel	Left Wing Panel
Run 1199	9.85°	9.85°
Run 1291	9.52°	9.04°
Run 1334	9.05°	10.05°

The symmetry or asymmetry of the wing stall is also evident in the C_l and C_{WM} data of figure 13. For Run 1334, C_l increases at α_{st} indicating that the right wing panel has stalled. Note that the data of figure 13(b) show that, for Run 1334, the break in the C_{WM} vs. α curve at α_{st} = 9.05° is significantly different between the right and left wing panels. C_{WM} of the right wing sharply decreases at α_{st} whereas C_{WM} of the left wing continues a gradual increase in C_{WM} with increasing α. The C_{WM} value for the left wing panel decreases at α = 10.05°, where the PSP data had shown the separation on the left wing panel had reached the leading-edge flap hingeline. The data of Run 1291 has similar behavior although the left wing panel stalls first. In contrast, the data for Sets 1 and 2 do not indicate one wing stalling before the other. For Sets 1 and 2, the data do not show a sharp increase or decrease in C_l at α_{st}, nor a sharp slope change in C_{WM} for either wing at α_{st}. Thus, the force/moment data agree with the PSP data in that neither wing panel is dominant in the wing stall process.

The repeatability analysis was also conducted on the C_p data. Figure 16 shows the data repeatability analysis for the left wing panel for nominal angles of attack of 8°, 9°, 10°, and 12°. At $\alpha \sim 8°$, before abrupt wing stall occurs, the pressure data has very little data scatter between the 8 runs of data. However, at α = 9° and $\alpha \sim 10°$, the 2σ value (95% confidence level) for the C_p data increases over the wing spar at mid-span. This observation corresponds to the fact that the location of the separation in this α-range varies for each run as indicated in the PSP data of figures 12, 14, and 15. However, at α = 11°, the 2σ value of the pressure coefficient data have decreased sharply. This observation corresponds to the separation having reached the leading-edge flap hingeline on both wing panels as noted in the PSP data of figures 12, 14, and 15.

The repeatability analysis shows a substantial increase in the data scatter (i.e., a loss in the repeatability of the data) in the angle of attack range where abrupt wing stall occurs. Abrupt wing stall can occur within a 1° α-range, is random (neither right or left dominant), and can occur symmetrically or asymmetrically. This random nature of the abrupt wing stall was also observed throughout the F/A-18E/F full-scale aircraft development program for more than one aircraft.

RMS Measurements

The fact that the same flap-set configuration installed at different times within a wind-tunnel test entry can stall at slightly different angles is indicative of the sensitive and dynamic nature of abrupt wing stall. Another approach to capturing the level of unsteadiness occurring over the wing panels was to use RMS (root mean square) instrumentation that calculated running values of RMS for the respective signals. This value of RMS was then recorded as a time-averaged measurement in the same manner as the static data. Figure 17 show the time-averaged measurement of RMS, denoted by the subscript rms, for each of the six balance components and the two wing-root bending-moment gauges for runs from Sets 1 and 2. The RMS instrumentation was not in use when runs in Sets 3 and 4 were conducted.

Figure 17 also shows the statistical data generated from the baseline data set. Note that the normal force and axial force coefficients (C_N and C_A, respectively) are plotted instead of C_L and C_D since C_N and C_A are the balance component signals recorded through the RMS boards. The repeatability analysis data are presented in two forms in upper plots of figure 17. The first form is the plot of the averaged data with a shaded area representing the 2σ of the data set. The second form is a line plot of the 2σ variable shown on the right axis. The scale for the right axis has been scaled up to show features of the 2σ value with respect to angle of attack.

Figure 17 shows the data over $-2° < \alpha < 12°$. Note that at the lower angles of attack, $\alpha < 6°$, both the time-averaged measured RMS and 2σ variable are fairly constant with increasing angle of attack. This trend would indicate that the model is not experiencing unsteady forces/moments. Indeed, for $\alpha < 9°$, the model was not observed to be vibrating on the sting. At α = 6°, the time-averaged measured RMS and 2σ variables show slight increases, which then decrease at α = 7°. This spike in the RMS corresponds to the trailing-edge separation at the mid-span of the wing advancing from the trailing-edge flap onto the wing spar as seen in the PSP data of figure 12(a).

Recall from the *Static and PSP Data* section that the model would vibrate under dynamic loads for the angle of attack range of 9° to 10°. The data show a marked increase in the RMS of each coefficient (except for C_A and C_y) at this angle of attack range. This sharp increase in RMS corresponds to an increase in the 2σ value from repeatability analysis conducted on the baseline data set. Since an increase in RMS denotes an increase in unsteadiness of that signal from the balance or strain gage, the increase in 2σ (which denotes an increase in data scatter between the 8 data runs) can also be interpreted to indicate an increase in unsteadiness in the flow over the wings.

Time History Measurements

Another approach to capturing the level of unsteadiness of the flow over the wing panels was to record the time histories of the instrument signals. Thus, a complete dynamic analysis could be conducted as was done on the baseline configuration in reference 4. This discussion will compare the repeatability analysis and RMS measurements to the average and RMS of the time history for several parameters. Figure 18 combines the C_l data from the three separate sets of data on the baseline configuration. The three sets of data are as follows: 1) repeatability analysis data, 2) static data, and 3) time history data. The first data set uses the repeatability analysis conducted for the baseline data set from the PSP test runs. The average and 2σ values, calculated from the 8 runs of data, are shown here. The static data and time history data are from one run of data (Run 20) for which static data and the time histories of several instruments were recorded. The second data set uses the static (or time-averaged value) of C_l. The RMS of the rolling moment balance component as measured through the RMS board is also shown as part of the static data set. For the third data set, an average of C_l was derived from the time history data. This average was subtracted from each data point of the time history data and the resulting values were used to calculate standard deviation, or RMS, for the time history data.

The average C_l derived from the time history of run 20 agrees well with the static (time-averaged) value of C_l. Note that both values of C_l fall within the 2σ band of the repeatability analysis. Also note that the RMS derived from the time history and the RMS measured as a time-averaged parameter agree very well in terms of magnitude and trend with angle of attack. However, the most striking observation is the trend of the RMS from the time history with respect to angle of attack. While the magnitude of the 2*RMS parameter is considerably more than that of the 2σ value, both parameters significantly increase over a very small angle of attack range ($8.5° < \alpha < 9°$) and maintain an elevated level for about an α increment of $1.5°$ ($9° < \alpha < 10.5°$) before returning to a lower value.

A similar comparison was made for the surface pressure coefficient data with mixed results. Figure 19 shows the C_p data from the three data sets defined above at several angles of attack. The time history data set consists of the 15 unsteady pressure transducers on the left wing. The 15 unsteady pressure transducers were the only pressure transducers routed through the RMS boards so the time-averaged data set only has RMS data for 15 of the pressure ports. The data of figure 19(a) at $\alpha = 5°$ show that the average C_p data, derived from the time history data of the unsteady pressure transducers, agree well with the static C_p data. The standard deviation data from all three data sets are small and indicate very little unsteady effects. At $\alpha = 6°$, the C_p derived from the time history agrees well with the static C_p data. Also, the 2*RMS values from both the time-averaged and time history data sets indicate a sharp increase in unsteadiness. This result corresponds to an increase in the 2σ value derived from the repeatability analysis. As discussed above, this activity is probably due to the separation moving from the trailing-edge flap onto the wing spar as seen in the PSP data of figure 12(a).

The repeatability analysis data show that once the angle of attack was increased to 7°, the 2σ value decreased sharply to a similar value as that observed before $\alpha = 6°$. In contrast, the 2*RMS data show that not all of the unsteady transducers returned to a low dynamic activity. Rather, those transducers near mid-chord and mid-span still experienced some dynamic activity, which is expected to be the result of mild shock oscillations that are identified in reference 4. This trend remained until $\alpha = 8.5°$ when the 2*RMS values for all of the transducers at mid-span increased and continued to increase with angle of attack. In fact at $\alpha = 10°$, the C_p and 2*RMS values from the time history data do not agree with the static data. In fact, these values are so greater than the plot maximums and thus do not appear in the plots. The 2σ value from the repeatability analysis do not experience a significant increase until $\alpha = 9°$ and are smaller in comparison to the time history data. The time history measurements are clearly more sensitive to the approach of abrupt wing stall than the repeatability analysis, which is to be expected since all of the data in the baseline data set has been passed through a low-pass frequency filter before being measured by the data system. Note that at $\alpha = 11°$ (figure 20(h)), after the mid-wing has stalled, both the 2σ and 2*RMS data return to low values seen before the dynamic activity was encountered at $\alpha = 6°$.

LESSONS LEARNED

The technical approach taken to observe and analyze the unsteady abrupt wing stall occurring on the 8% F/A-18E/F Model has yielded not only information on the wing stall process, but also on the experimental techniques used. The lessons learned are listed here:

1. The angle of attack increment required to capture the abrupt stall process was 0.5°. A test conducted using conventional increments of α (1 or greater) would have missed the critical features of the phenomenon.

2. Trenches for pressure tubing and wiring should be limited to the lower surface of wings to minimize the impact of the fill material in the trenches during PSP testing.

3. The model has to be at room temperature before the PSP coat can be applied. The need for the model to cool down after running greatly increased down time in the wind tunnel between configuration changes.

4. The need to obtain wind-off data after 1, or at most 2, runs greatly increased the length of time needed to test one configuration.

5. Care and sensitivity to potential impacts on data is needed during the application of trip dots and other model features that might affect the aerodynamic performance of the leading-edge flaps.

6. Repeat runs should be included in a test program and can be used to clarify unsteady or repeatability issues.

CONCLUDING REMARKS

A wind tunnel test of a pre-production 8% F/A-18E model at M =0.90 was conducted in the NASA LaRC 16-ft TT to investigate on-surface flow physics during wing stall. The technical approach employed focused on correlating static (or time-averaged) and unsteady wind-tunnel test data to the unsteady wing-stall events using force, moment, pressure, and pressure-sensitive-paint measurements. The abrupt wing stall experienced by the 8% F/A-18E Model was observed to be an unsteady event ccurring when the separation, which had migrated forward from the trailing edge, rapidly advanced to the leading-edge flap hingeline for a very small increment in angle of attack. The angle of attack at which wing stall occurred varied, from run to run, over an 1° increment. The abrupt wing stall can occur simultaneously on both wing panels or asymmetrically. Asymmetric rolling moment occurs if the wing stall occurs asymmetrically. As angle of attack is further increased, both wing panels stall and the large roll asymmetries are significantly reduced.

Several techniques were used to capture abrupt wing stall in a conventional wind tunnel set-up. The pressure-sensitive-paint technique provided global looks at the flow structures occurring over the wing before and during wing stall. PSP data and wing-root bending-moment strain gages data provided insight to the asymmetry (or symmetry) of the abrupt wing stall process. A simple repeatability analysis was conducted on the static data from 8 runs on the pre-production F/A-18E configuration. The standard deviation (σ) value was observed to be an indicator of unsteadiness in the flow over the wing. The repeatability analysis provided a quick and inexpensive examination of the unsteady aerodynamic characteristics of abrupt wing stall. The repeatability analysis was surprisingly accurate when compared to unsteady measurements of pressures and rolling moment. This approach could be used to identify test conditions at which a more complex and detailed examination of unsteady data could be conducted.

REFERENCES

1. Hall, R., and Woodson, S: Introduction to the Abrupt Wing Stall (AWS) Program. AIAA-2003-0589, January, 2003.

2. Capone, F. J.; Bangert, L. S.; Asbury, S. C.; Mills, C. T. L.; and Bare, E. A.: The NASA Langley 16 Foot Transonic Tunnel - Historical Overview, Facility Description, Calibration, Flow Characteristics, and Test Capabilities. NASA TP 3521, 1995.

3. Schuster, David M.; and Byrd, James E.: Transonic Unsteady Aerodynamics of the F/A-18E at Conditions Promoting Abrupt Wing Stall. AIAA-2003-0593, January, 2003.

4. Sprinkle, D. R.; Obara, C. J.; Amer, T. R.; Leighty, B. D.; Carmine, M. T.; Burkett, C. G.; and Sealey, B. S: Langley 16-Ft. Transonic Tunnel Pressure Sensitive Paint System. NASA TM-2001-211017, 2001.

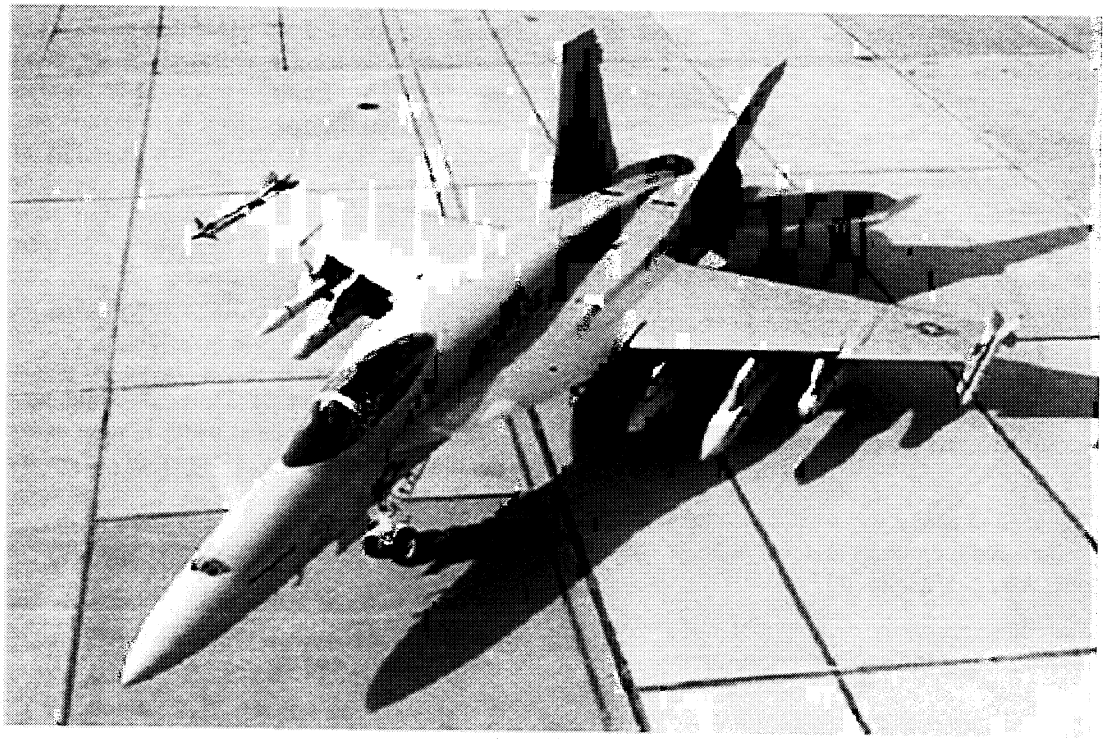

Figure 1. Photograph of the F/A-18E/F aircraft.

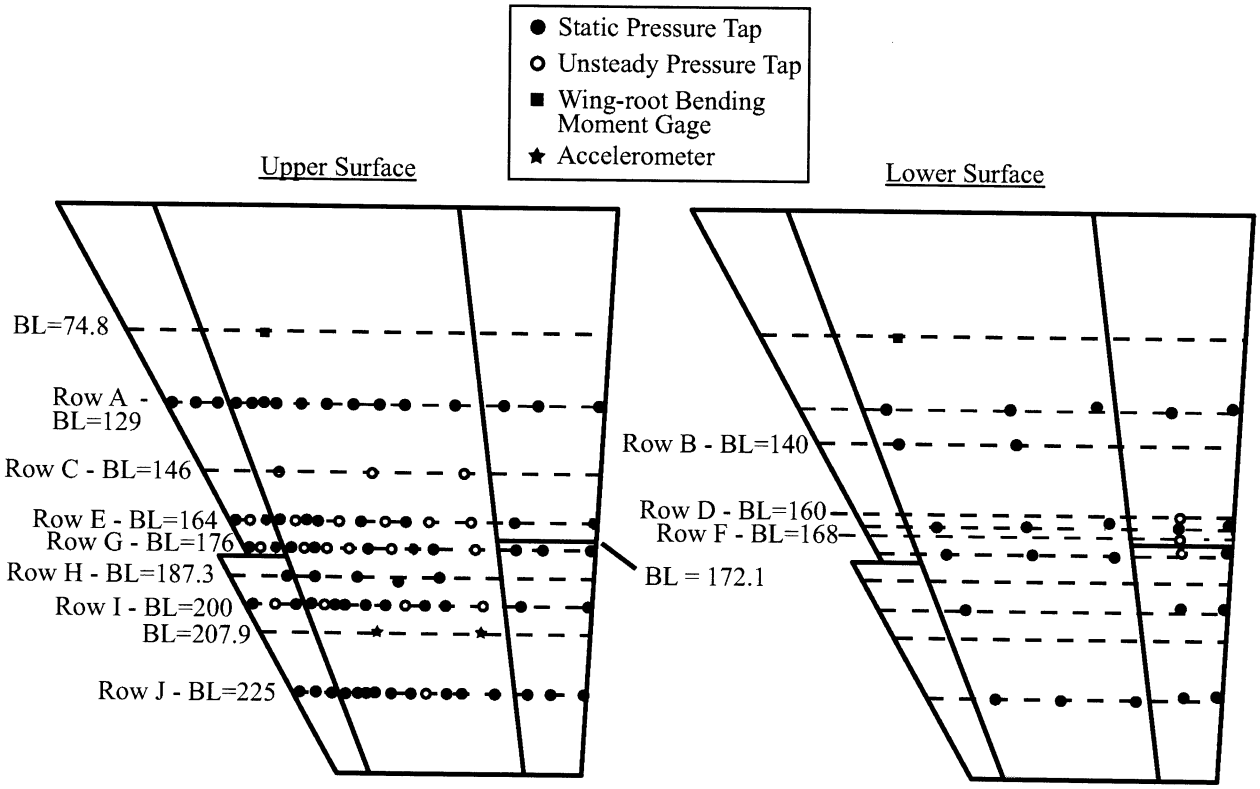

(a) Left heavily instrumented wing.

Figure 2. Sketches of the instrumented wings for the 8% F/A-18E Model. Full-scale dimensions are in inches.

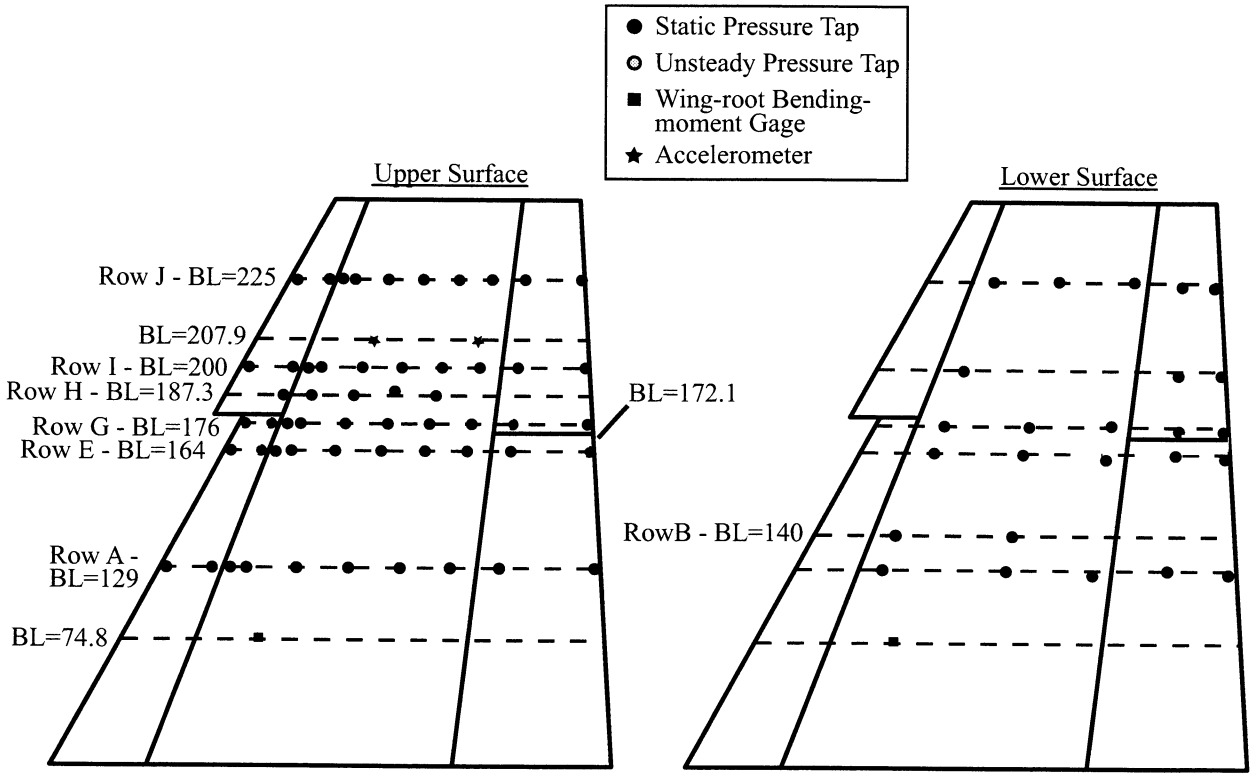

(b) Right instrumented wing.

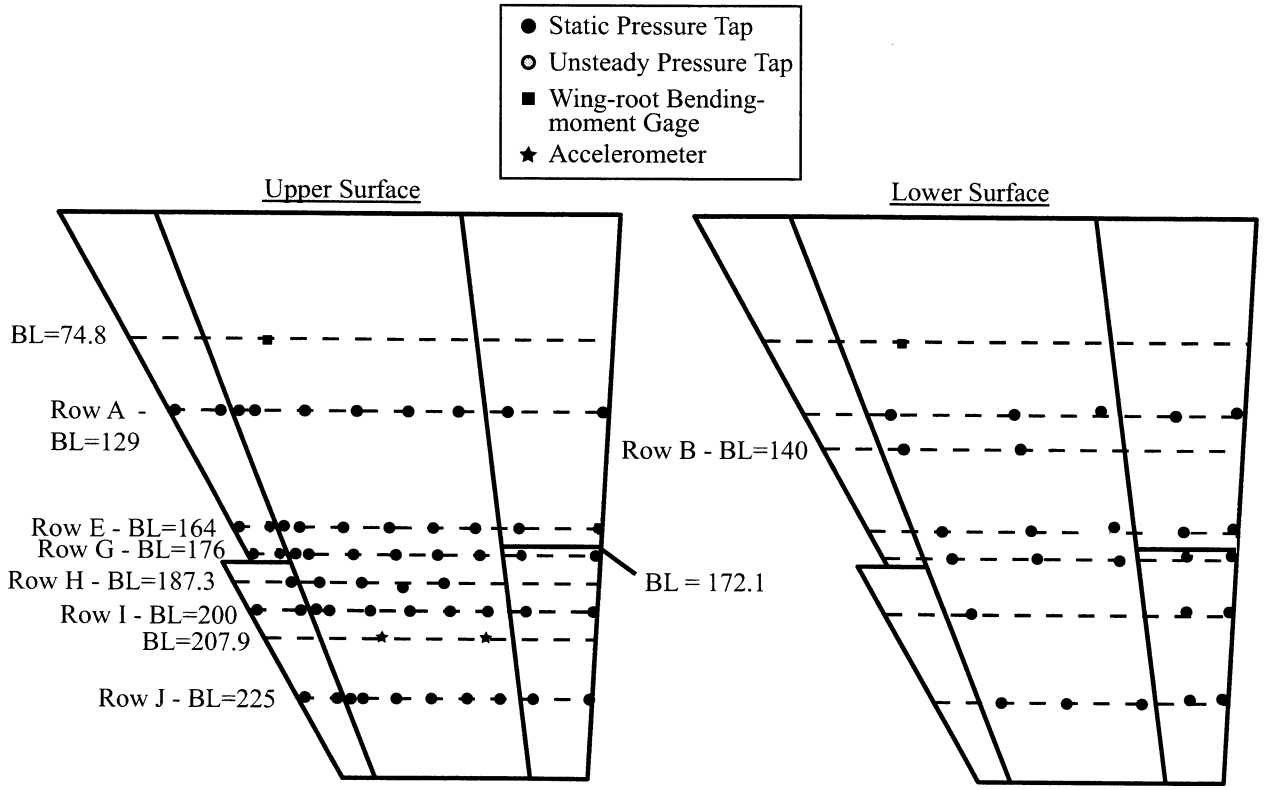

(c) Left lightly instrumented wing.

Figure 2. Concluded.

(a) Bottom view of model/sting/strut assembly.

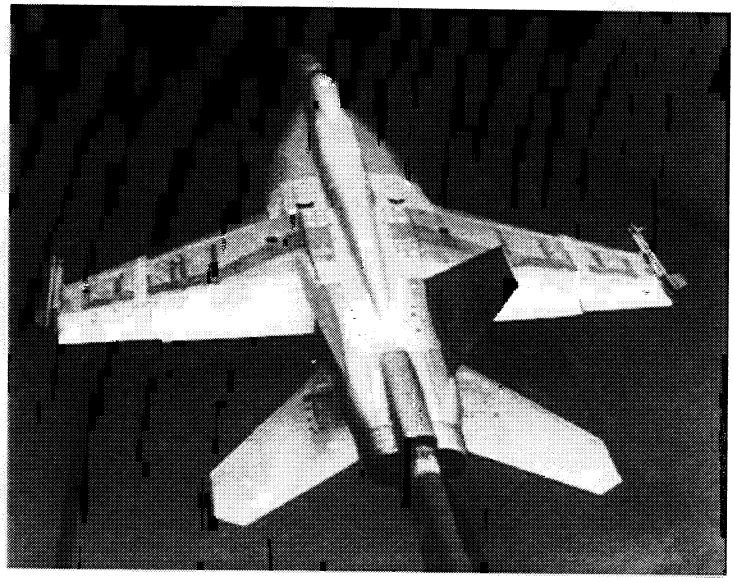

(b) Top view of model.

Figure 3. Photographs of the 8% F/A-18E Model in the 16-ft. TT.

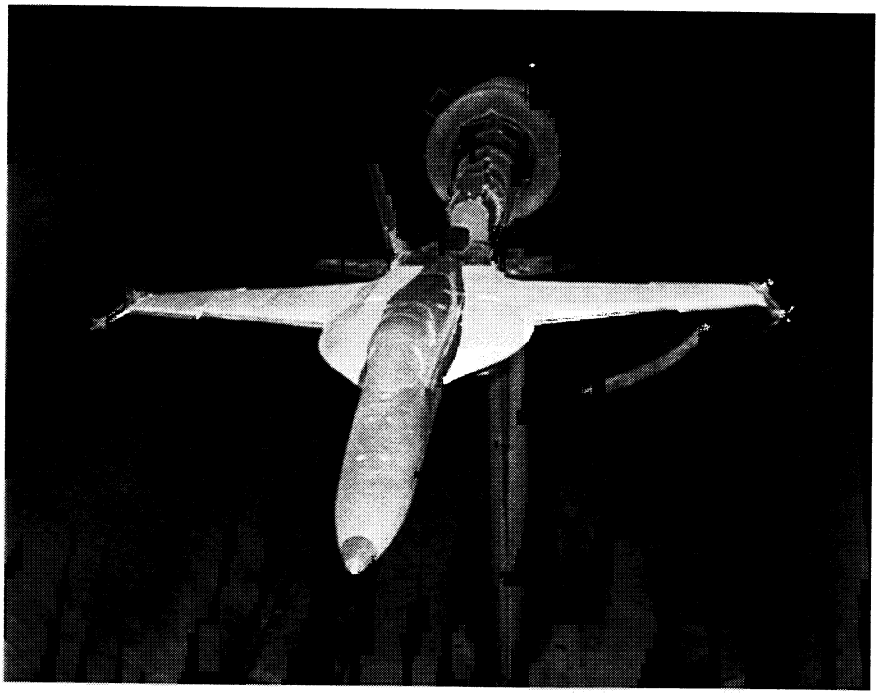

(a) Top view of model with PSP coat.

Figure 4. Photographs of PSP coat applied to the model.

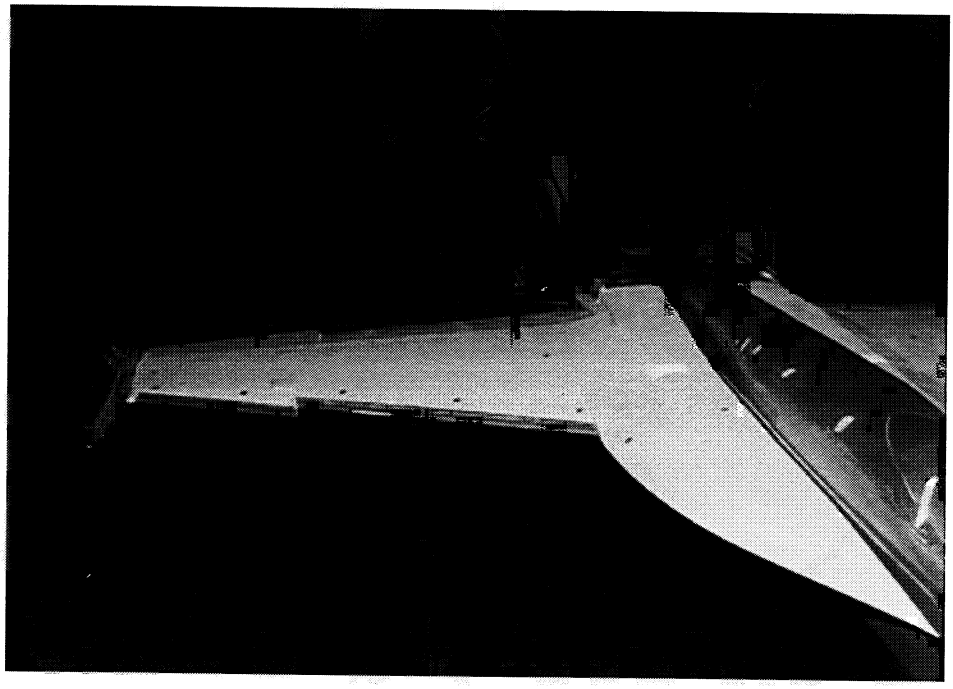

(b) Close-up view of right wing panel.

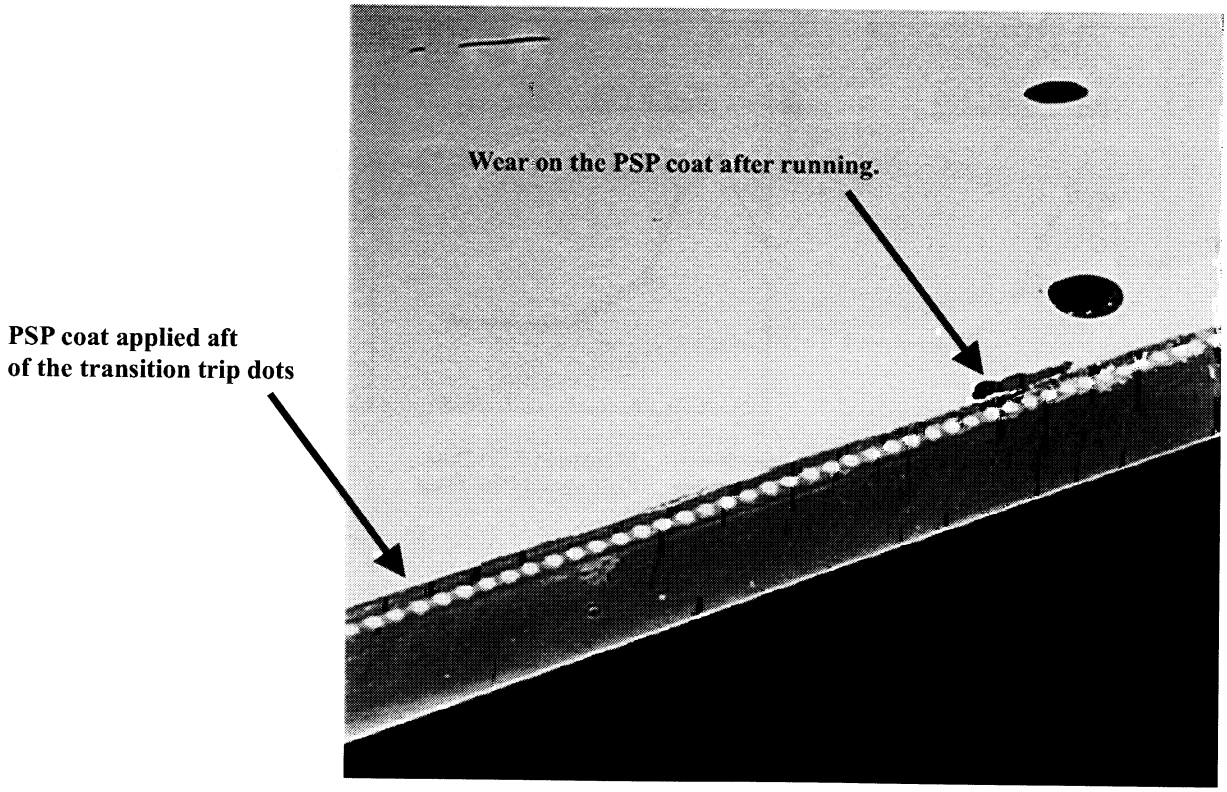

(c) Close-up view on wing leading-edge and trip dots.

Figure 4. Concluded.

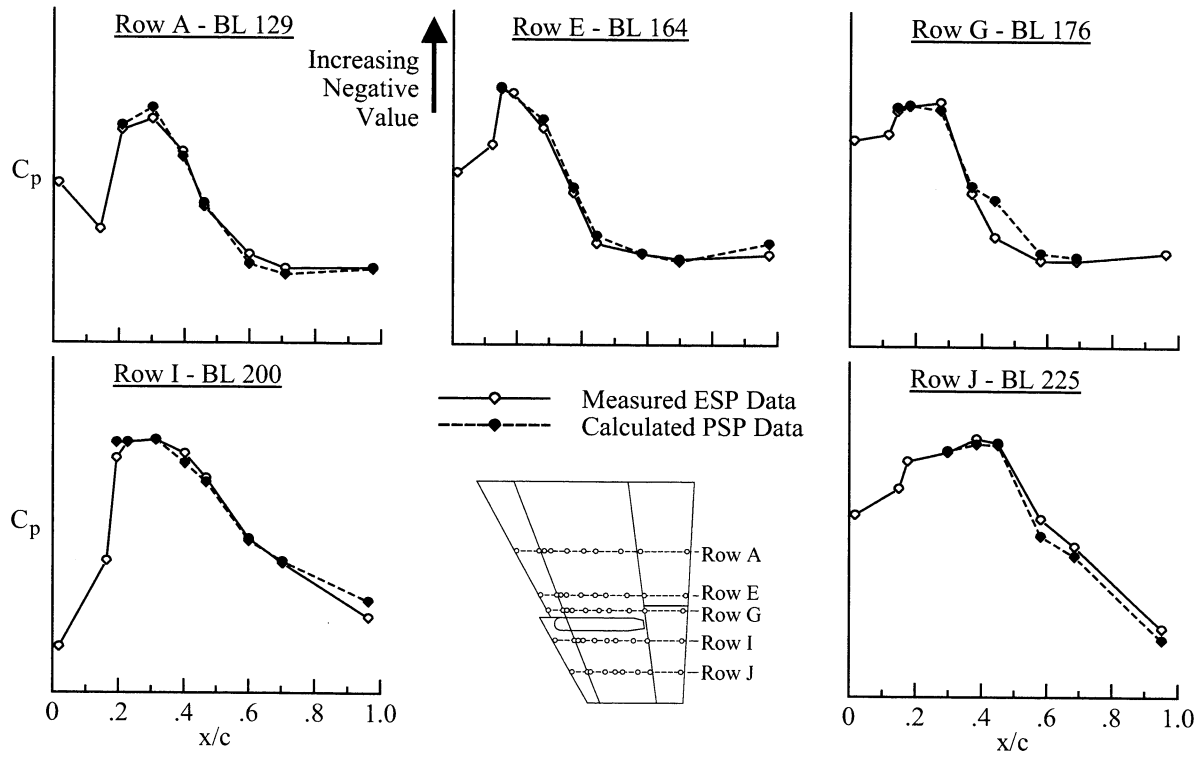

(a) Left wing data.

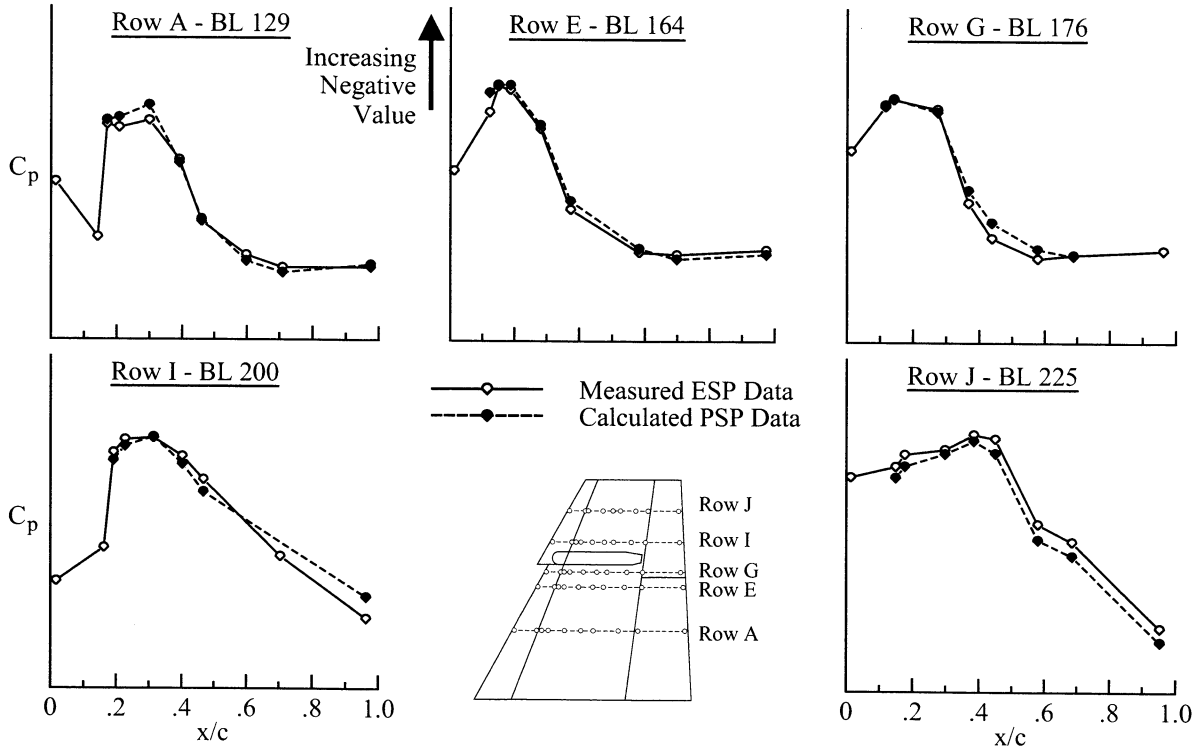

(b) Right wing data.

Figure 5. Comparison of surface pressure coefficients from measured ESP and calculated PSP data for the baseline configuration with 10°/10°/5° flaps at M=0.9 and α = 8.0° (run 1334).

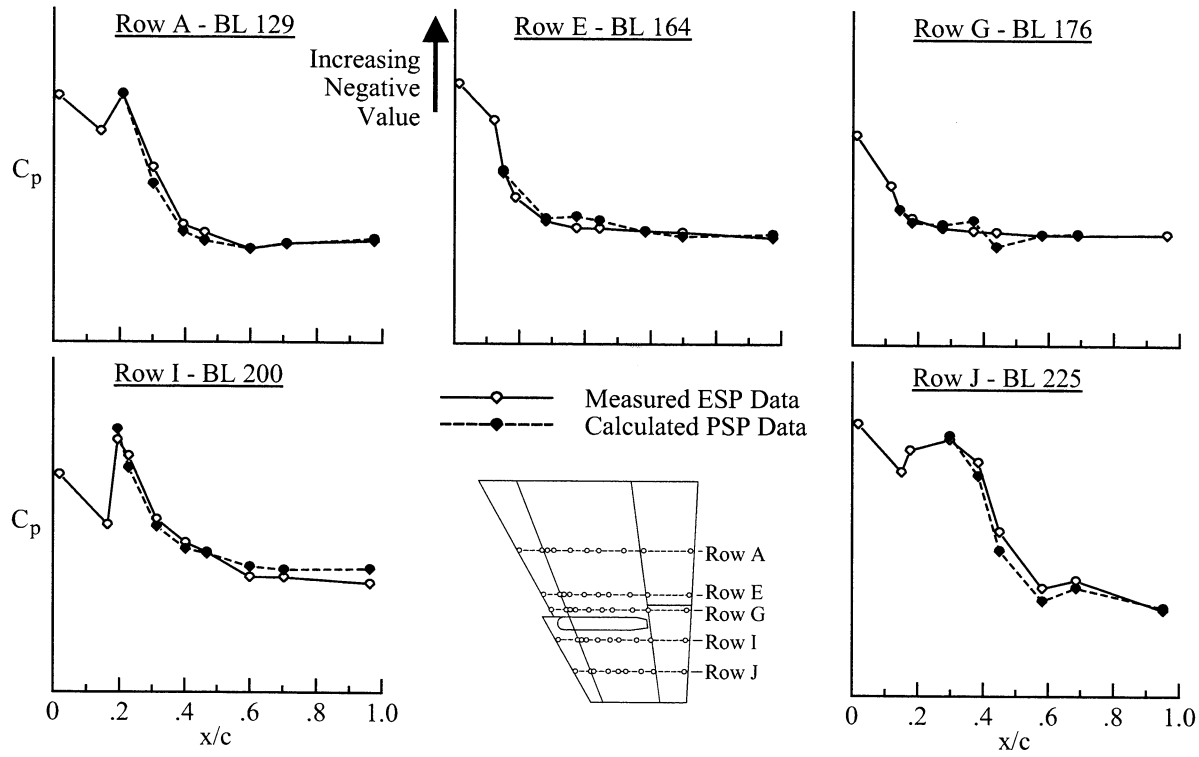

(a) Left wing data.

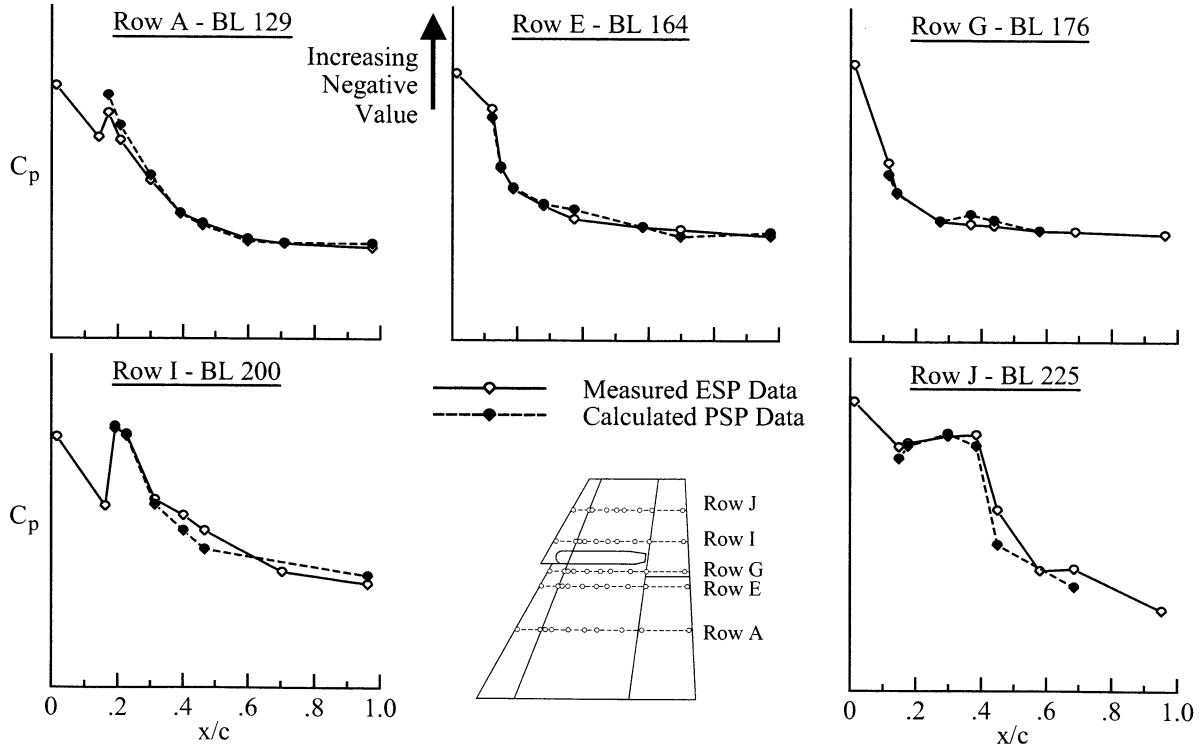

(b) Right wing data.

Figure 6. Comparison of surface pressure coefficients from measured ESP and calculated PSP data for the baseline configuration with 10°/10°/5° flaps at M = 0.9 and α = 10.0° (run 1334).

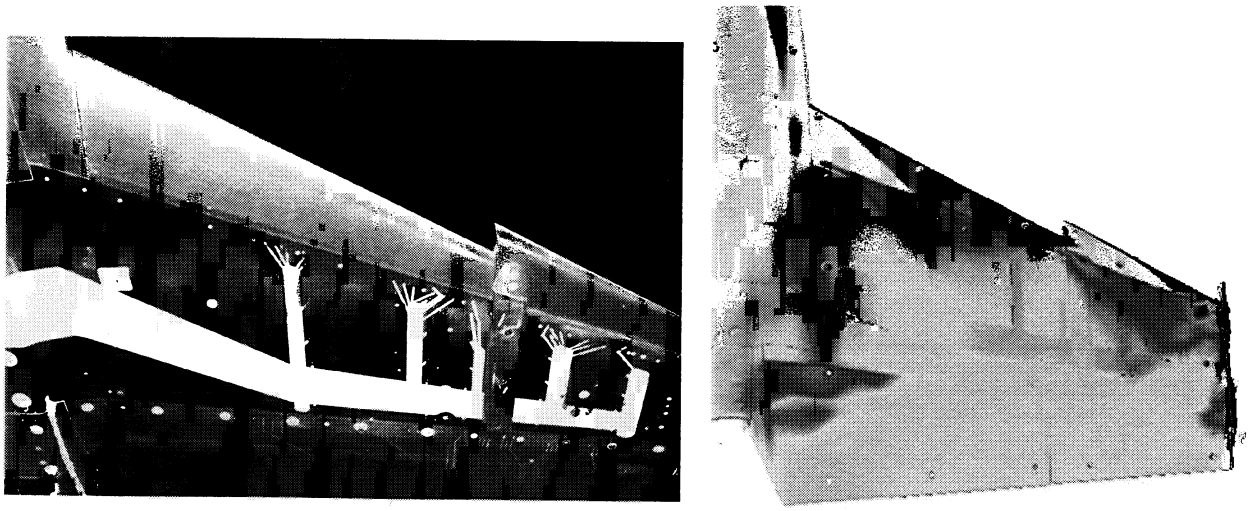

(a) Bare model - instrumentation trenches in white paint.

(b) PSP image for the baseline configuration with 10°/10°/5° flaps at M=0.9 and α=10.0° (run 1334).

Figure 7. The effect of trench fill material on the PSP image.

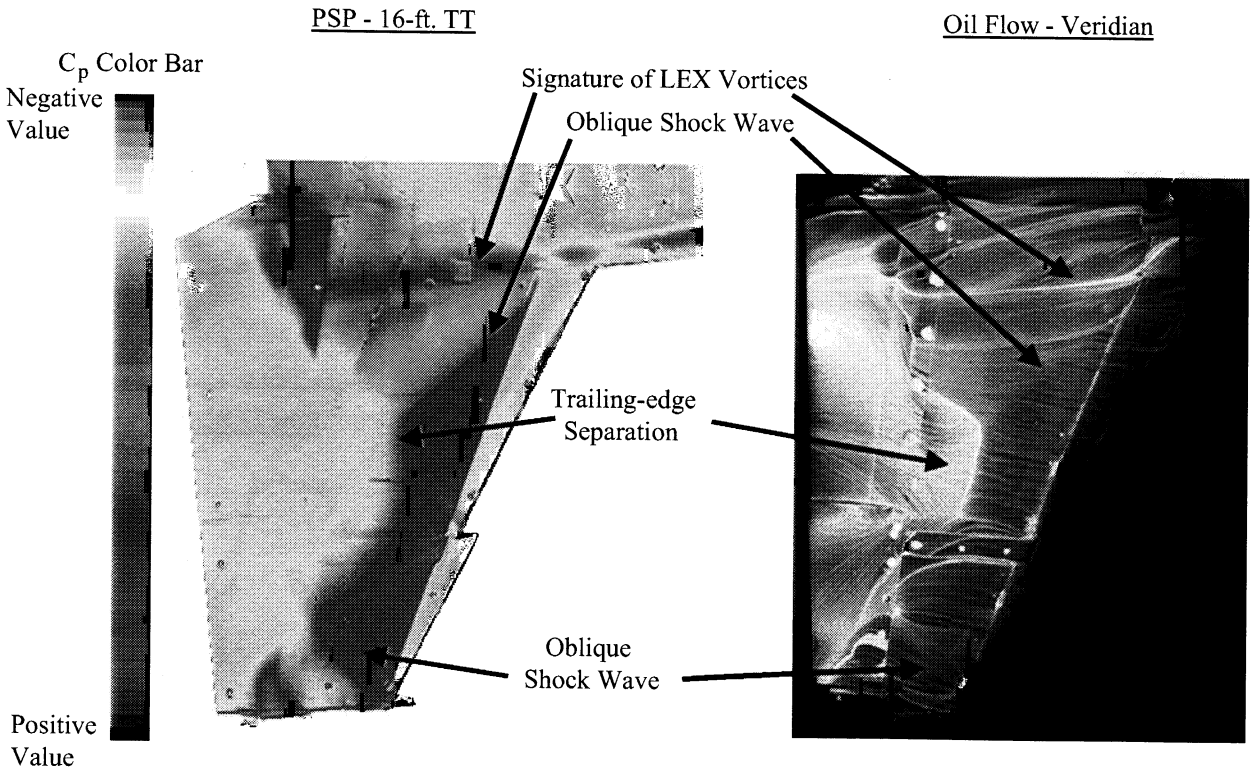

Figure 8. Comparison of PSP image and oil flow image on the baseline configuration with 10°/10°/5° flaps at M = 0.9 and α = 8.0° (run 1334).

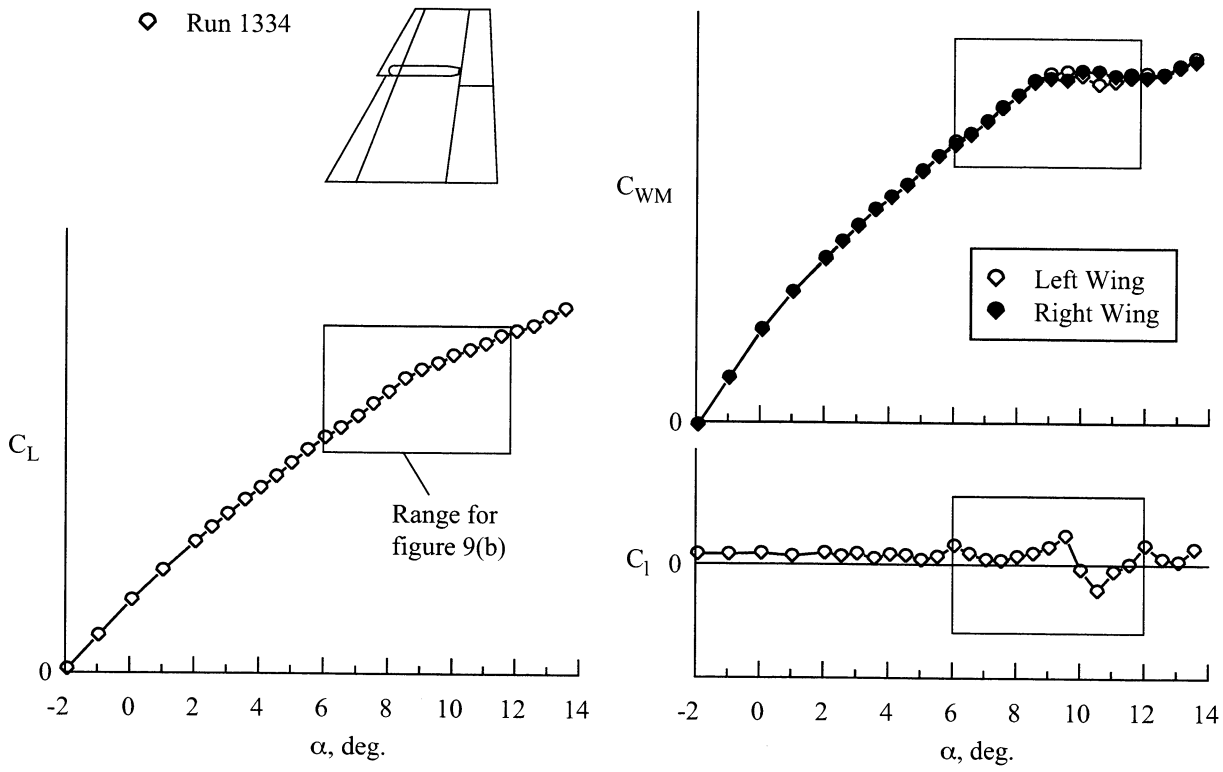

(a) $-2° < \alpha < 14°$.

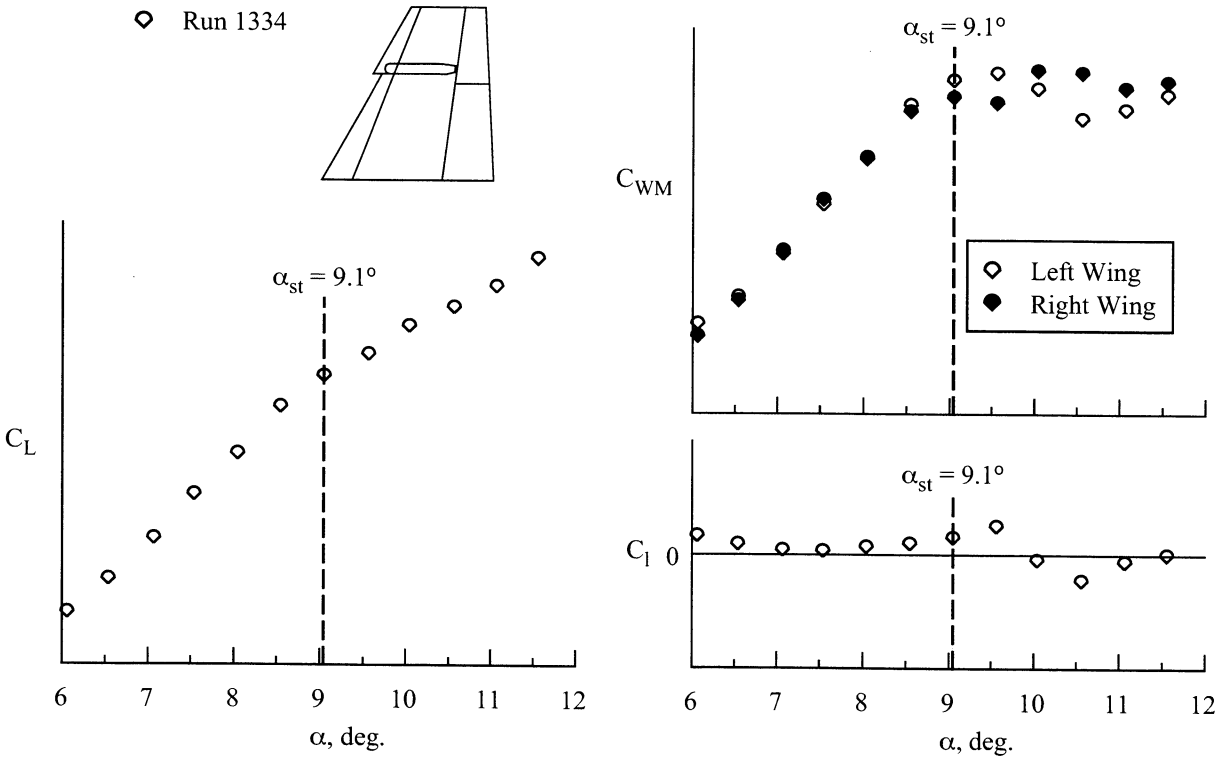

(b) $6° < \alpha < 12°$.

Figure 9. Lift, rolling moment, and wing-root bending-moment coefficient data for the baseline configuration with 10°/10°/5° flaps at M = 0.9 (run 1334).

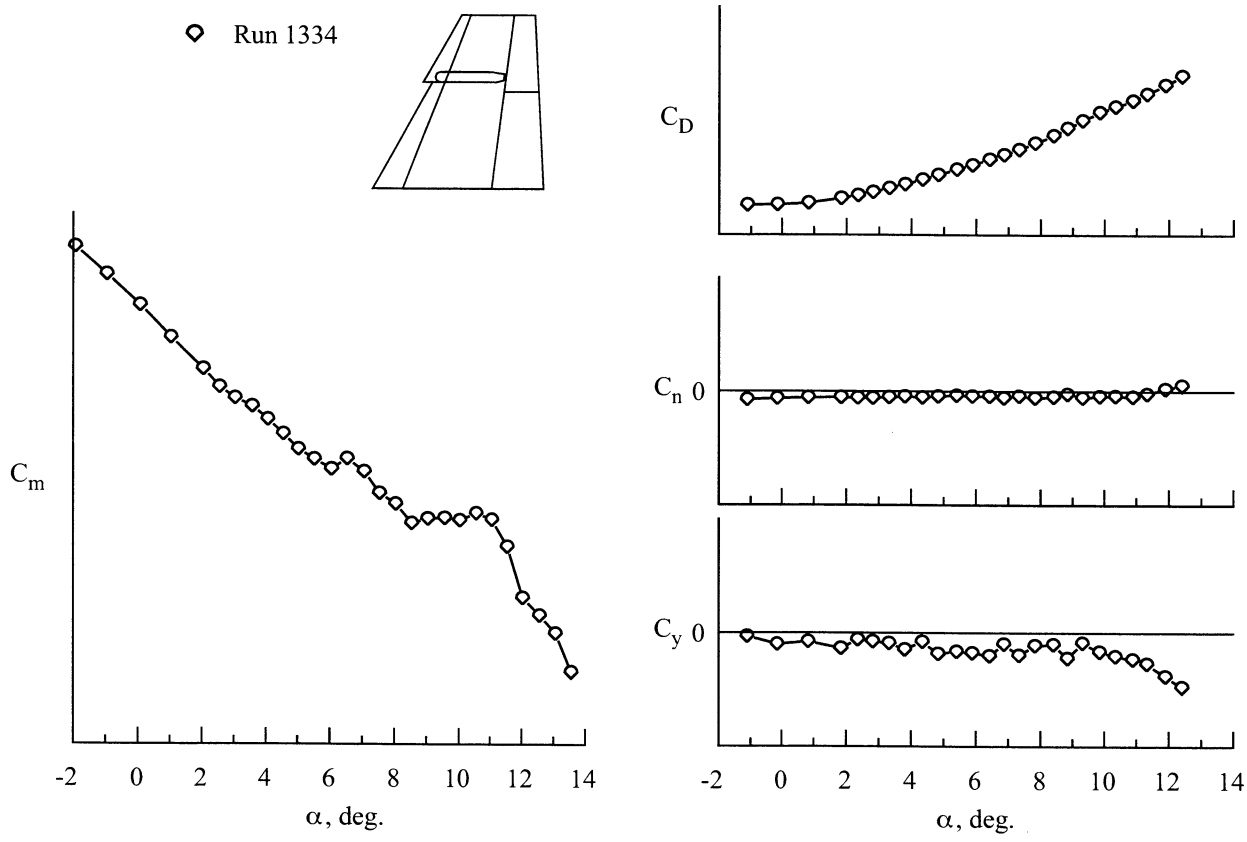

Figure 10. Pitching moment, side force, yawing moment, and drag coefficient data for the baseline configuration with 10°/10°/5° flaps at M = 0.9 and $-2° < \alpha < 14°$ (run 1334).

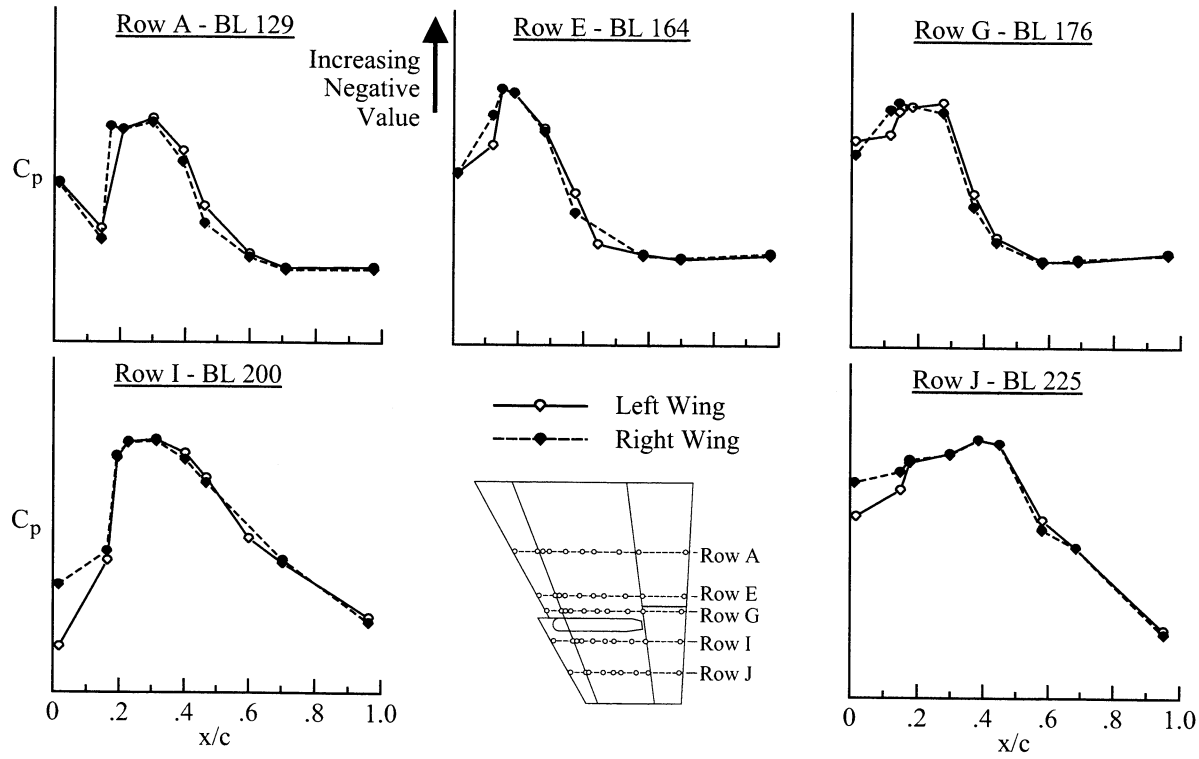

(a) $\alpha = 8.0°$.

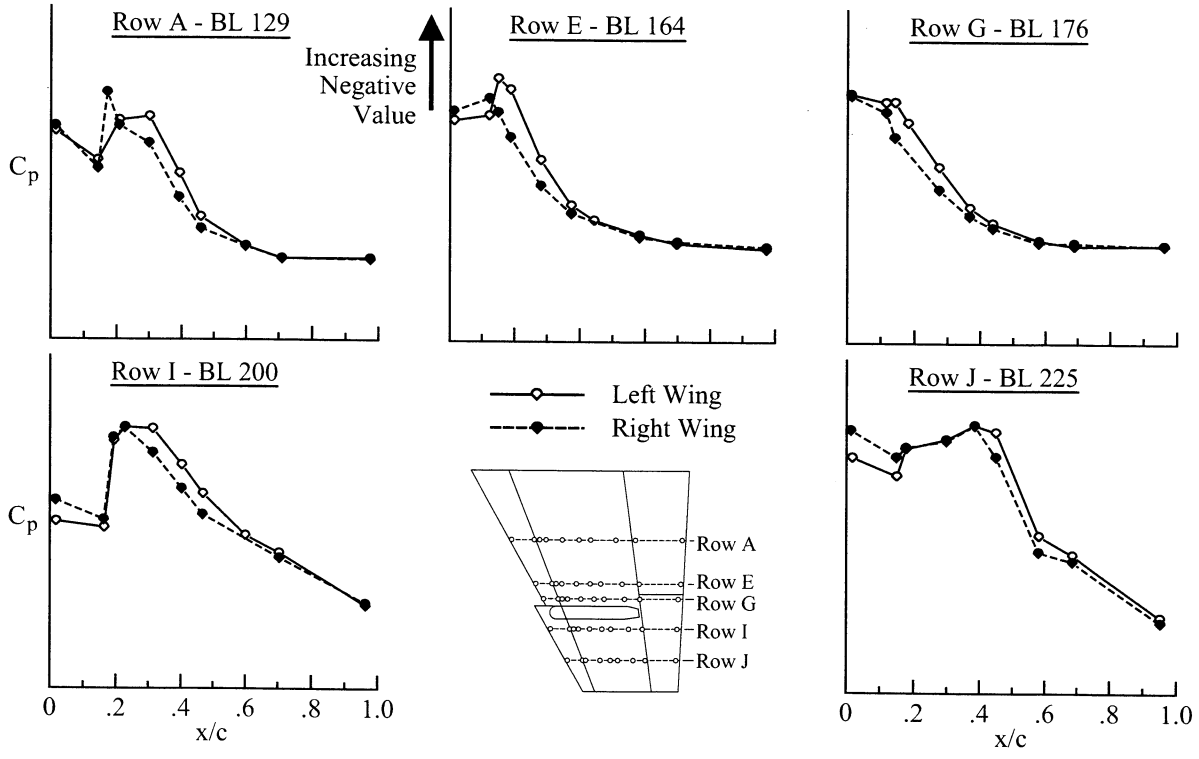

(b) $\alpha = 9.1°$.

Figure 11. Comparison of surface pressure coefficients from the left and right wing panels for the baseline configuration with 10°/10°/5° flaps at M = 0.9 at various α conditions (run 1334).

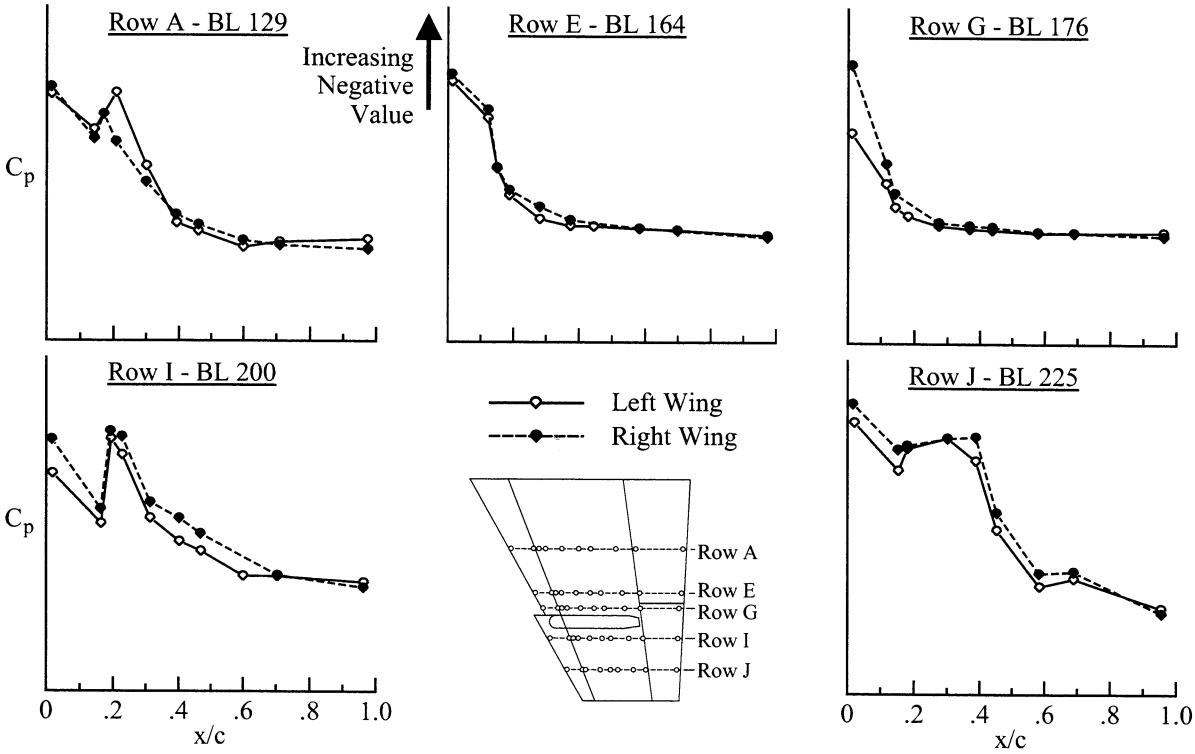

(c) $\alpha = 10.0°$.

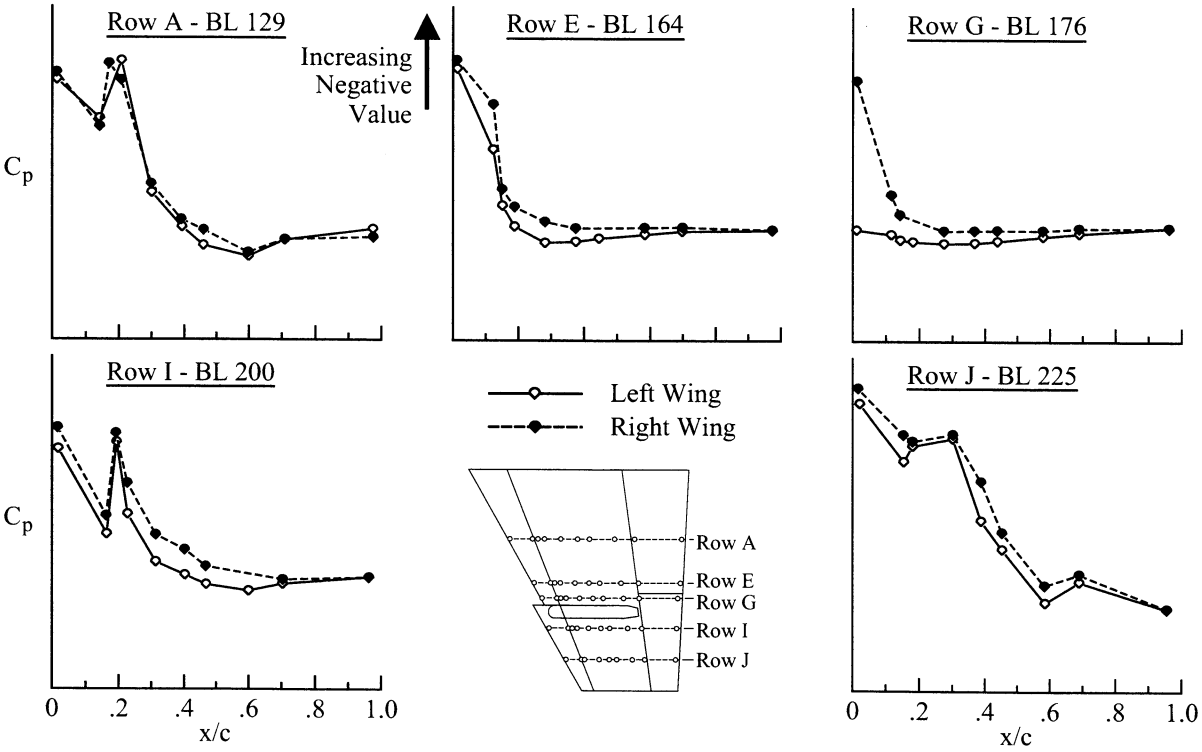

(d) $\alpha = 10.6°$.

Figure 11. Concluded.

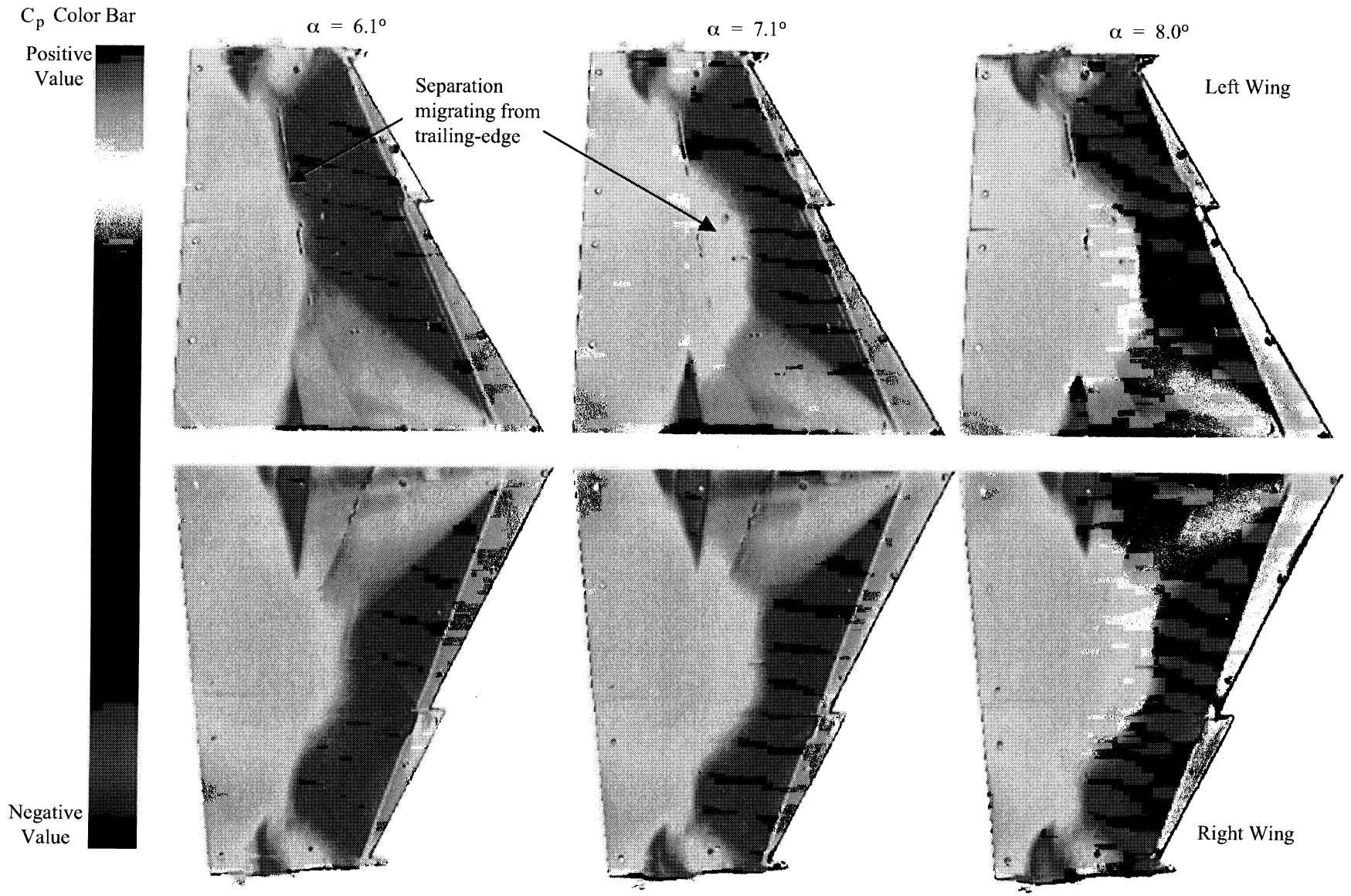

(a) α = 6.06°, 7.07°, 8.04°.

Figure 12. PSP data for the baseline configuration with 10°/10°/5° flaps at M = 0.9 and various α conditions (run 1334).

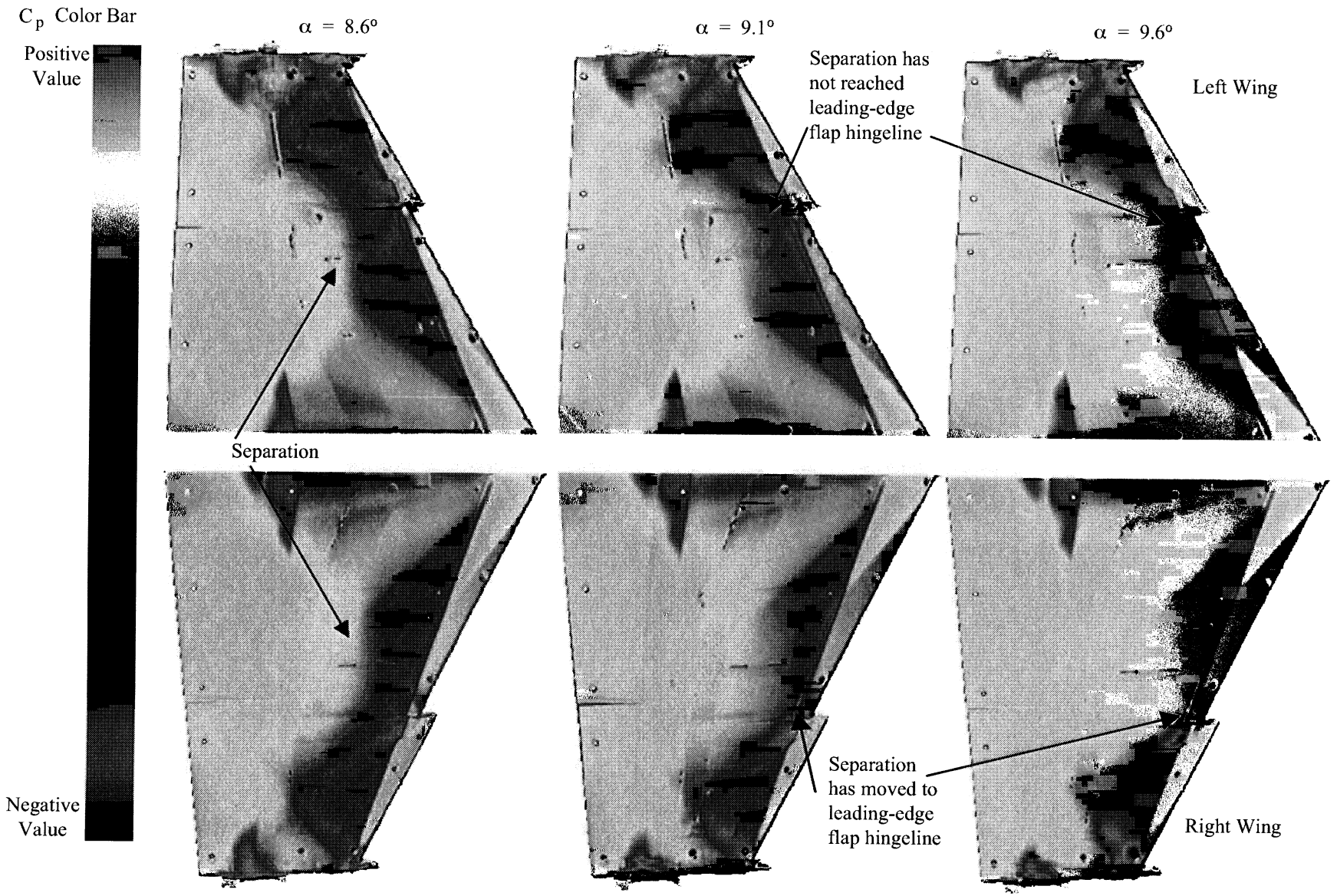

(b) α = 8.6°, 9.1°, 9.6°.
Figure 12. Continued.

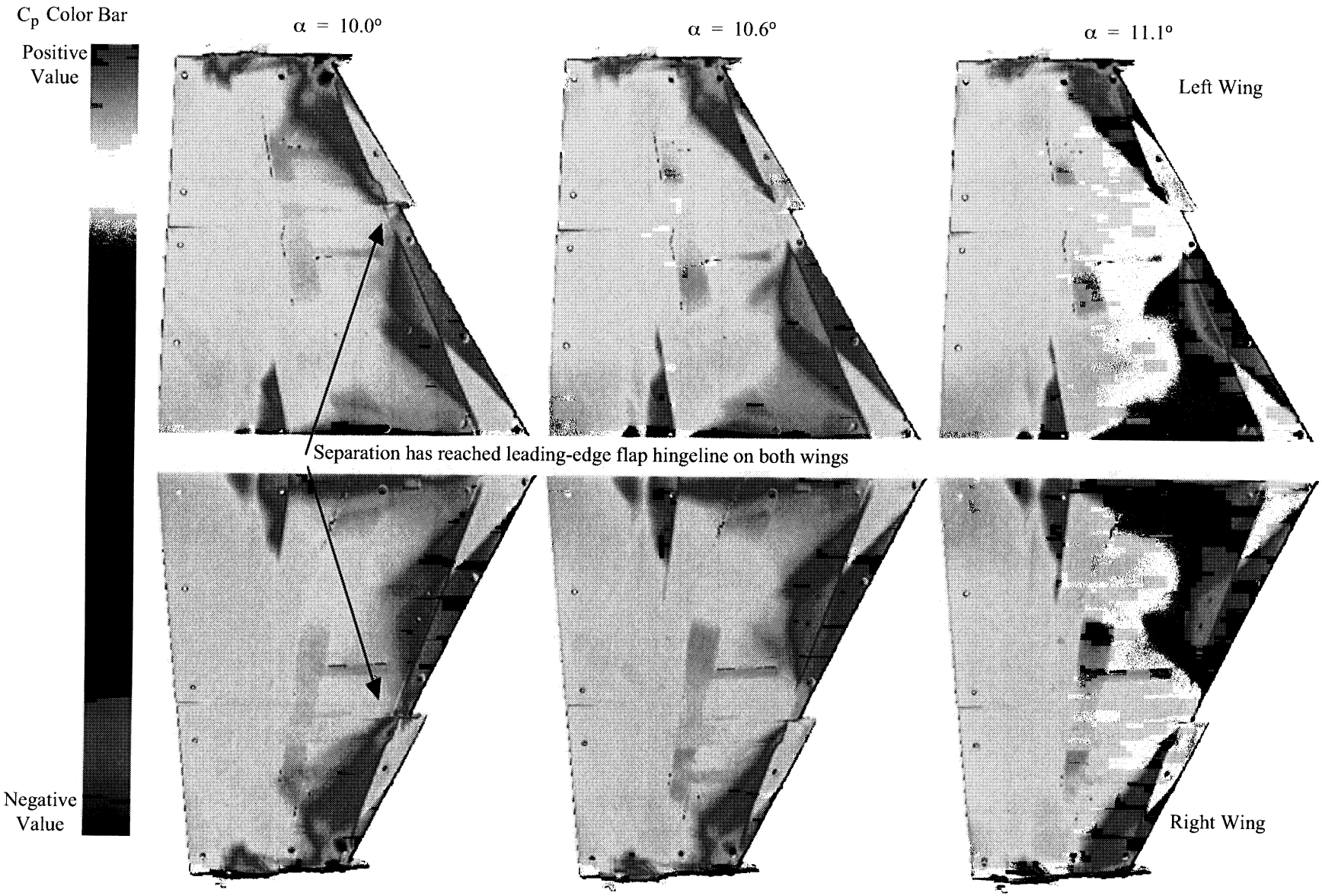

(c) α = 10.0°, 10.6°, 11.1°.

Figure 12. Concluded.

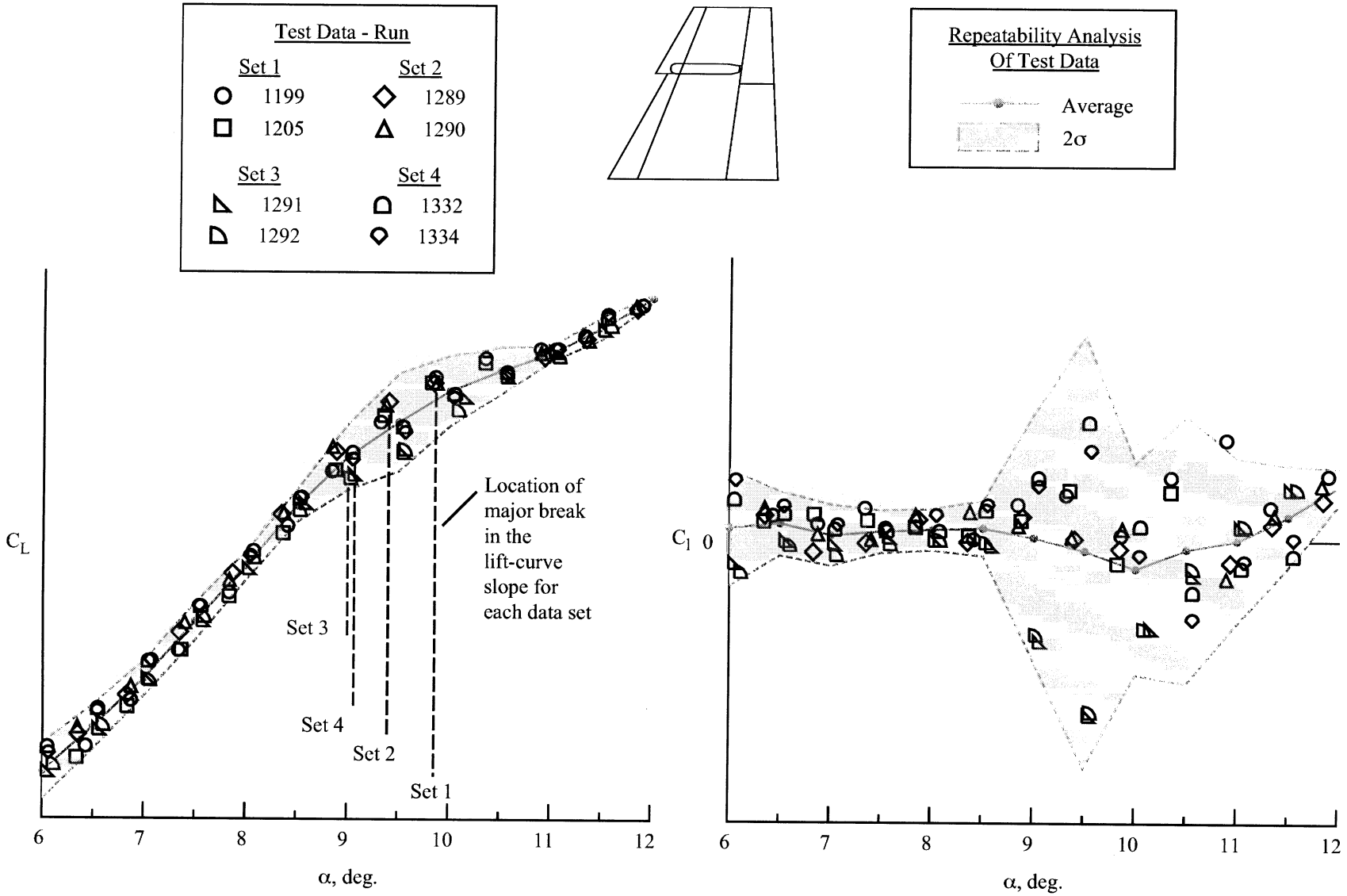

(a) C_L and C_l data.

Figure 13. Configuration aerodynamic coefficients and repeatability analysis for the eight runs on the baseline configuration with 10°/10°/5° flaps at M = 0.9.

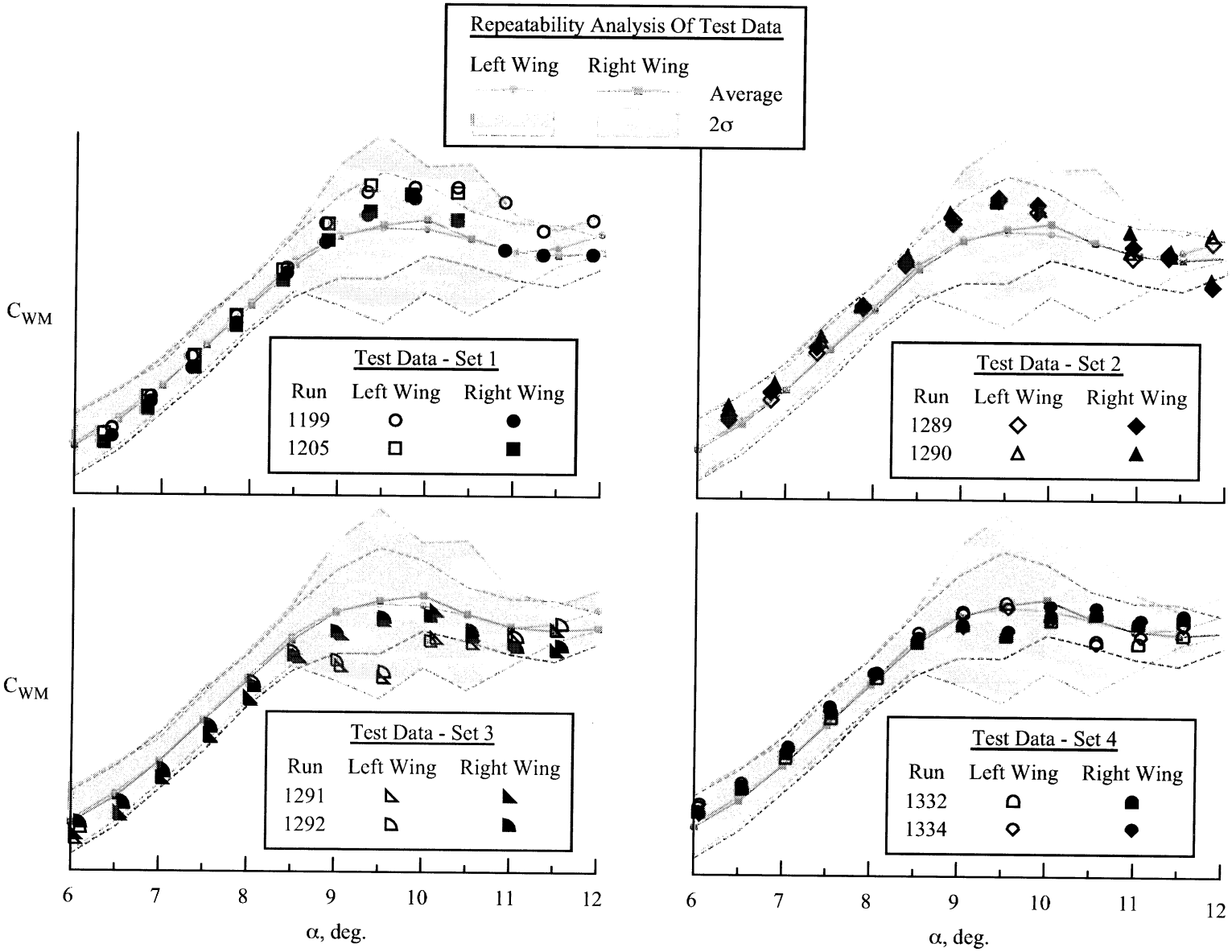

(b) C_{WM} data for the left and right wing panels.

Figure 13. Continued.

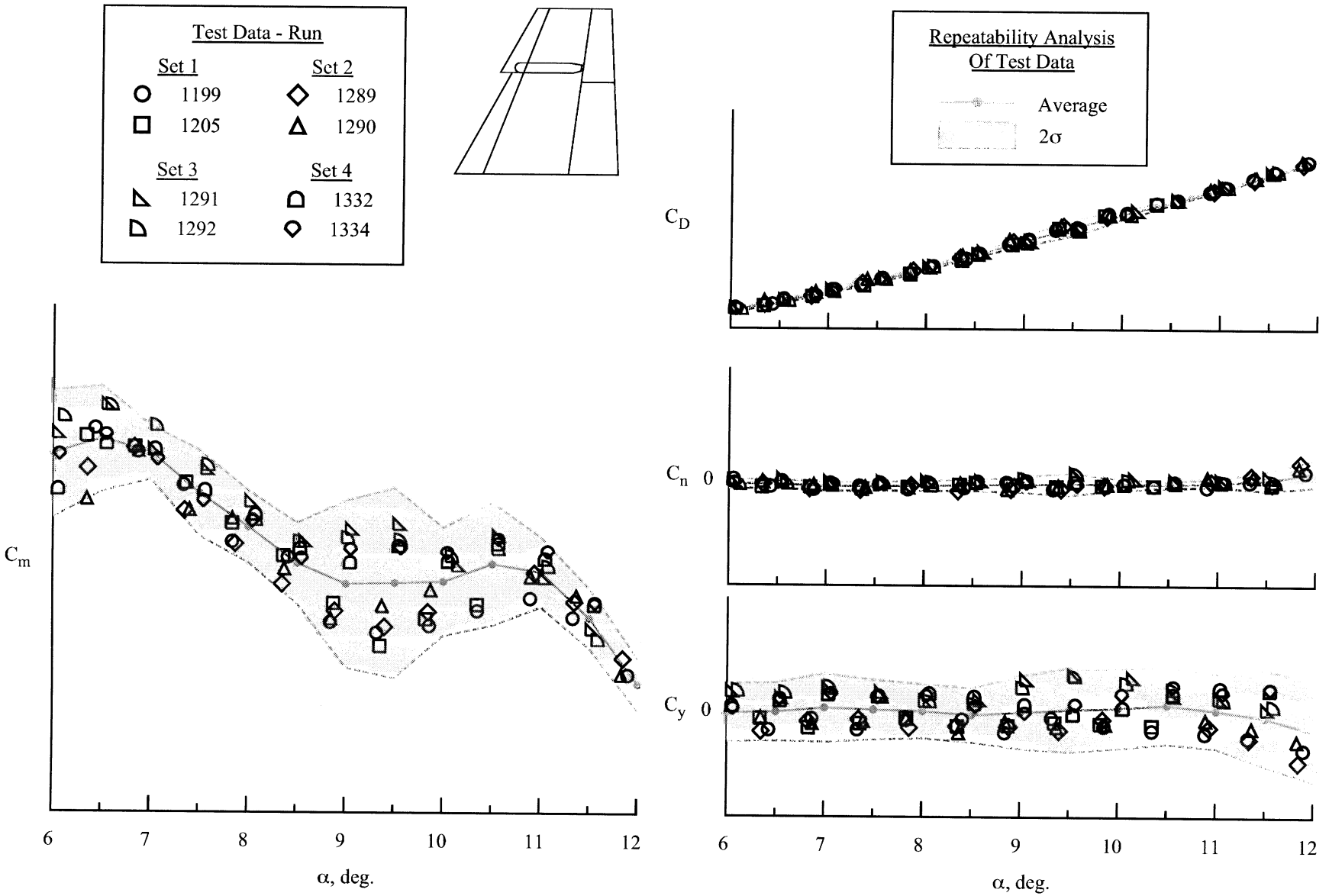

(c) C_m, C_D, C_n, and C_y data.

Figure 13. Concluded.

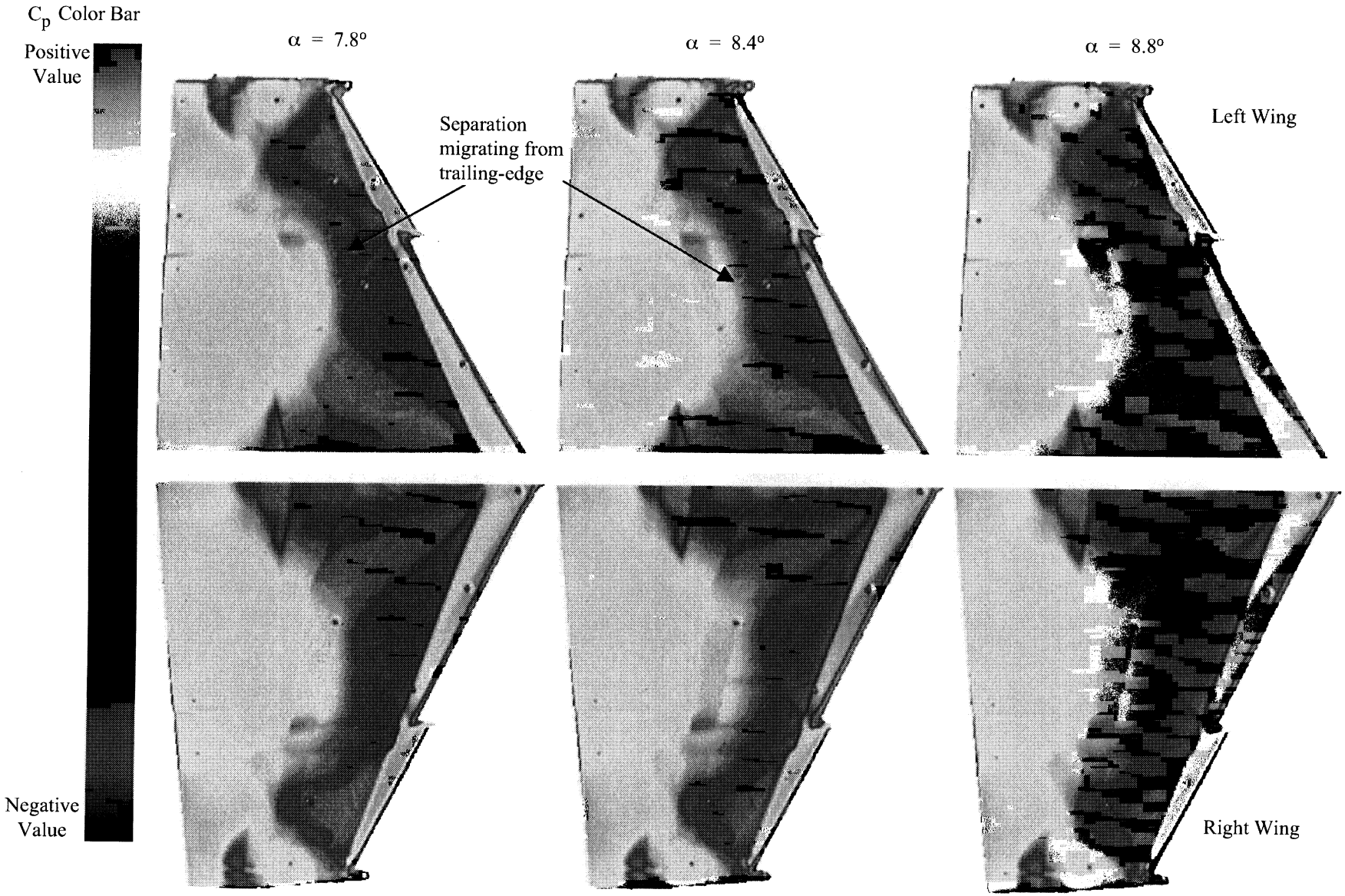

(a) α = 7.8°, 8.4°, 8.8°.

Figure 14. PSP data for the baseline configuration with 10°/10°/5° flaps at M = 0.9 and various α conditions (run 1199).

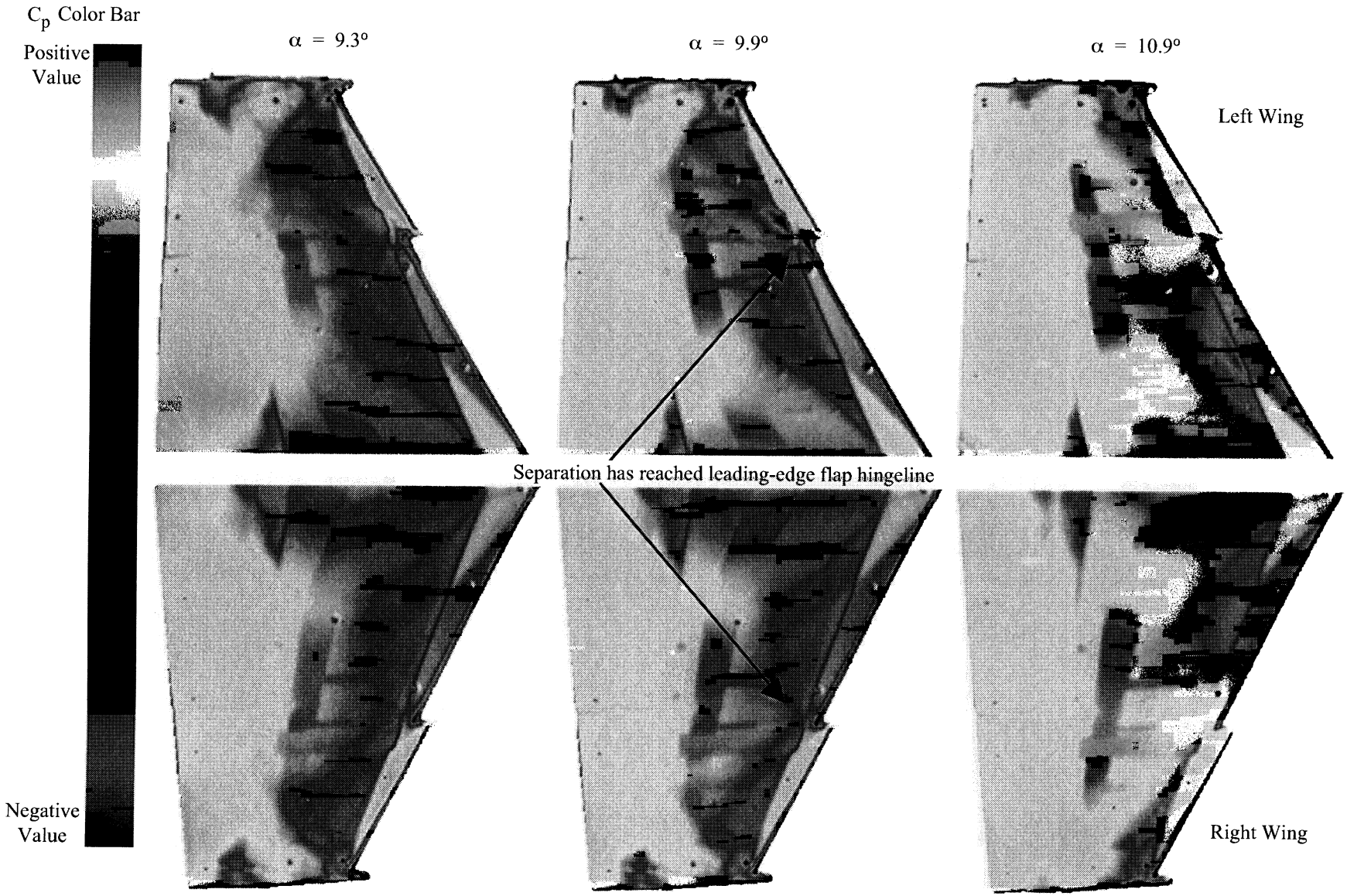

(b) α = 9.3°, 9.9°, 10.9°.

Figure 14. Concluded.

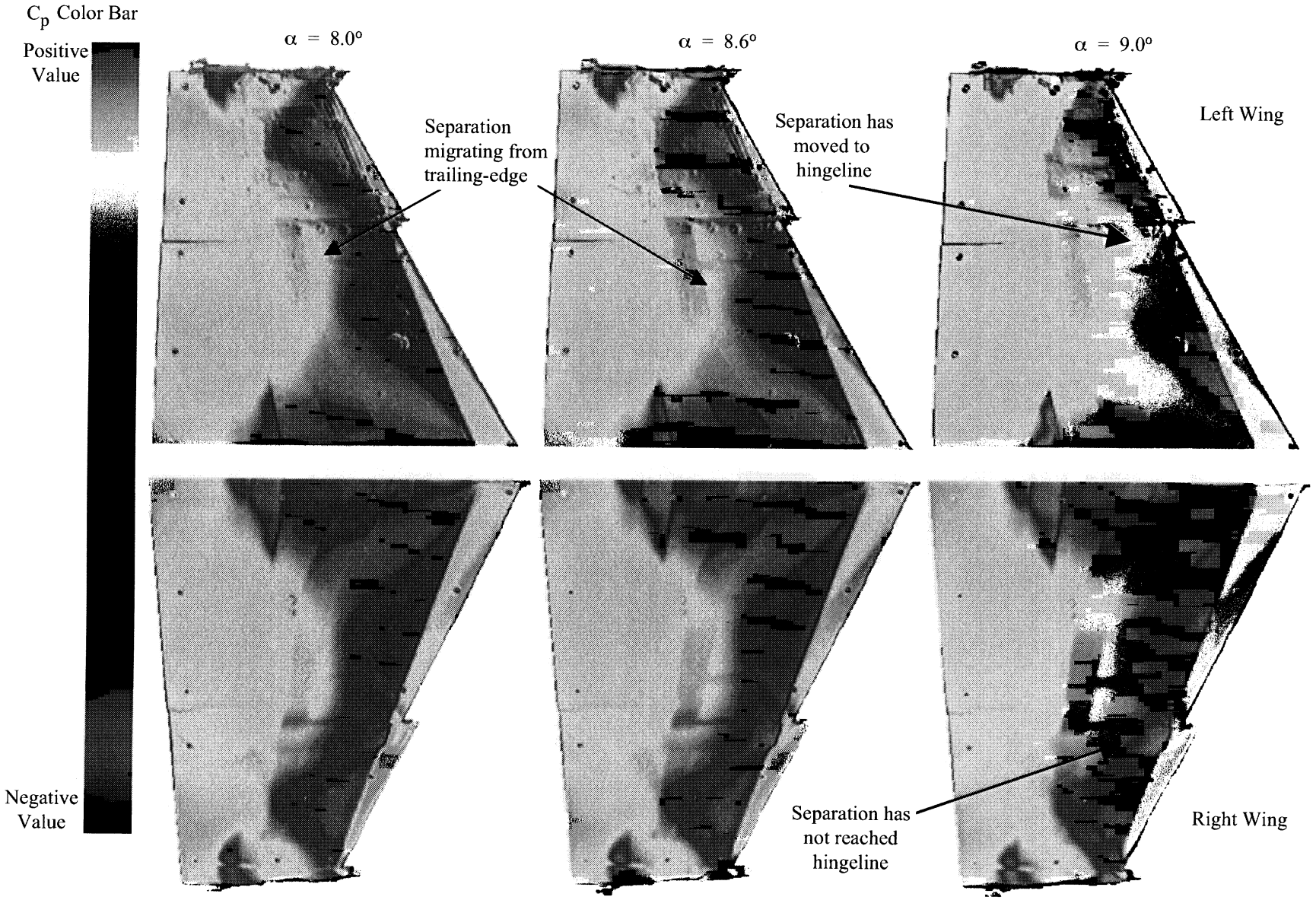

(a) α = 8.0°, 8.6°, 9.0°.

Figure 15. PSP data for the baseline configuration with 10°/10°/5° flaps at M = 0.9 and various α conditions (run 1291).

AIAA-2003-0591

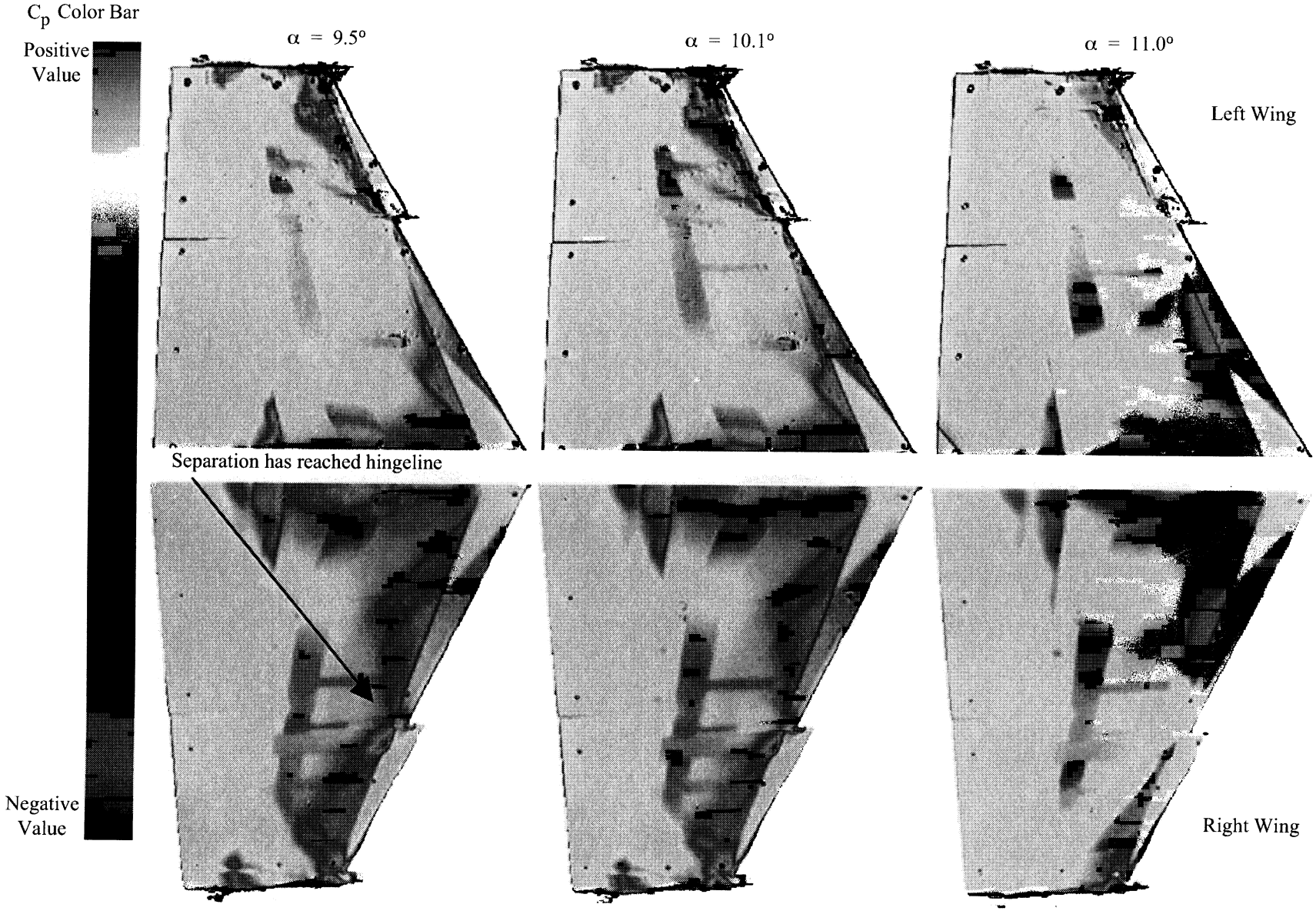

(b) α = 9.5°, 10.1°, 11.0°.

Figure 15. Concluded.

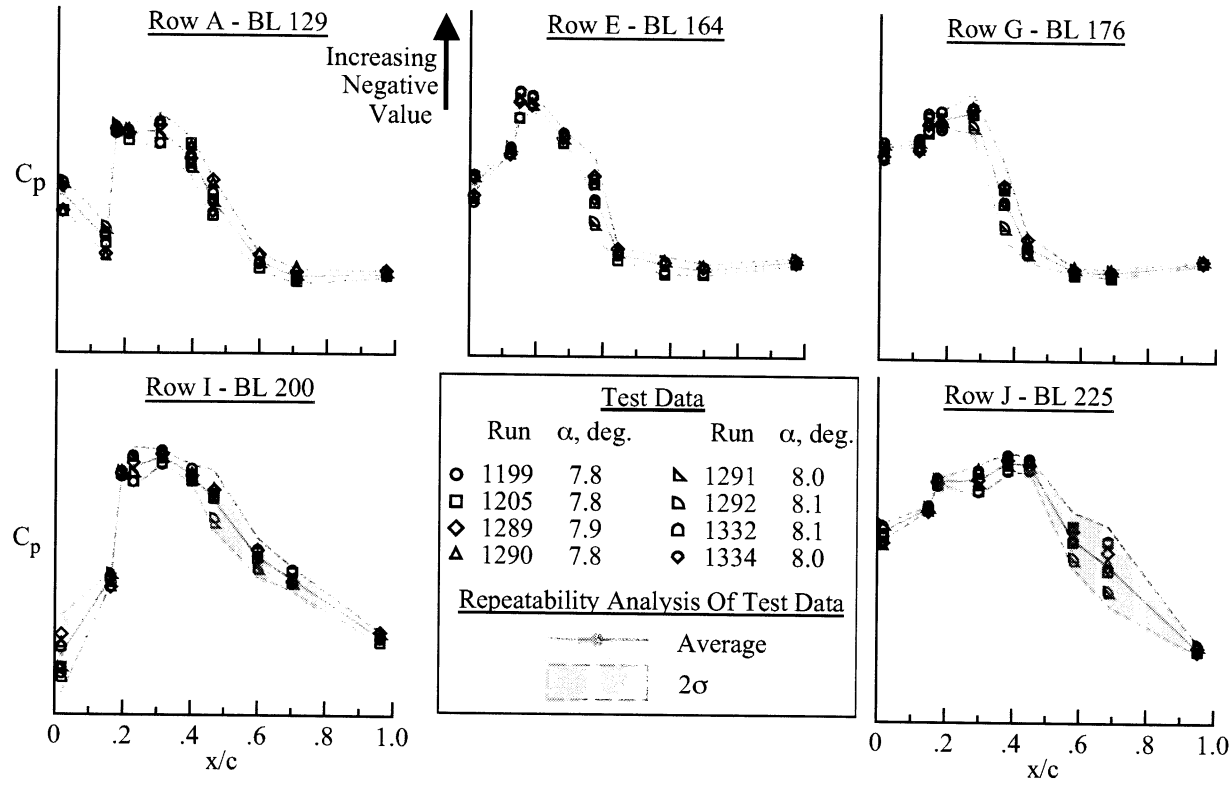

(a) $\alpha \sim 8°$.

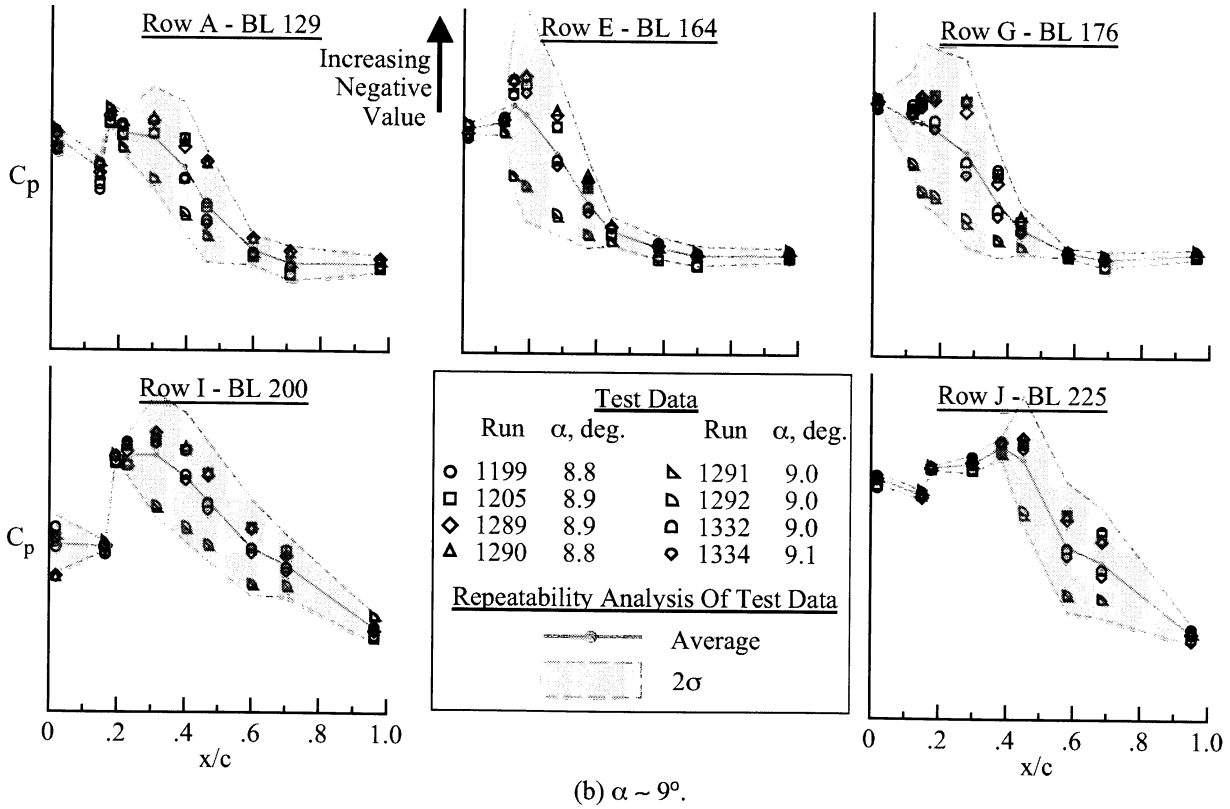

(b) $\alpha \sim 9°$.

Figure 16. Left wing surface pressure coefficient data and repeatability analysis for the eight runson the baseline configuration with 10°/10°/5° flaps at M = 0.9 at various α conditions.

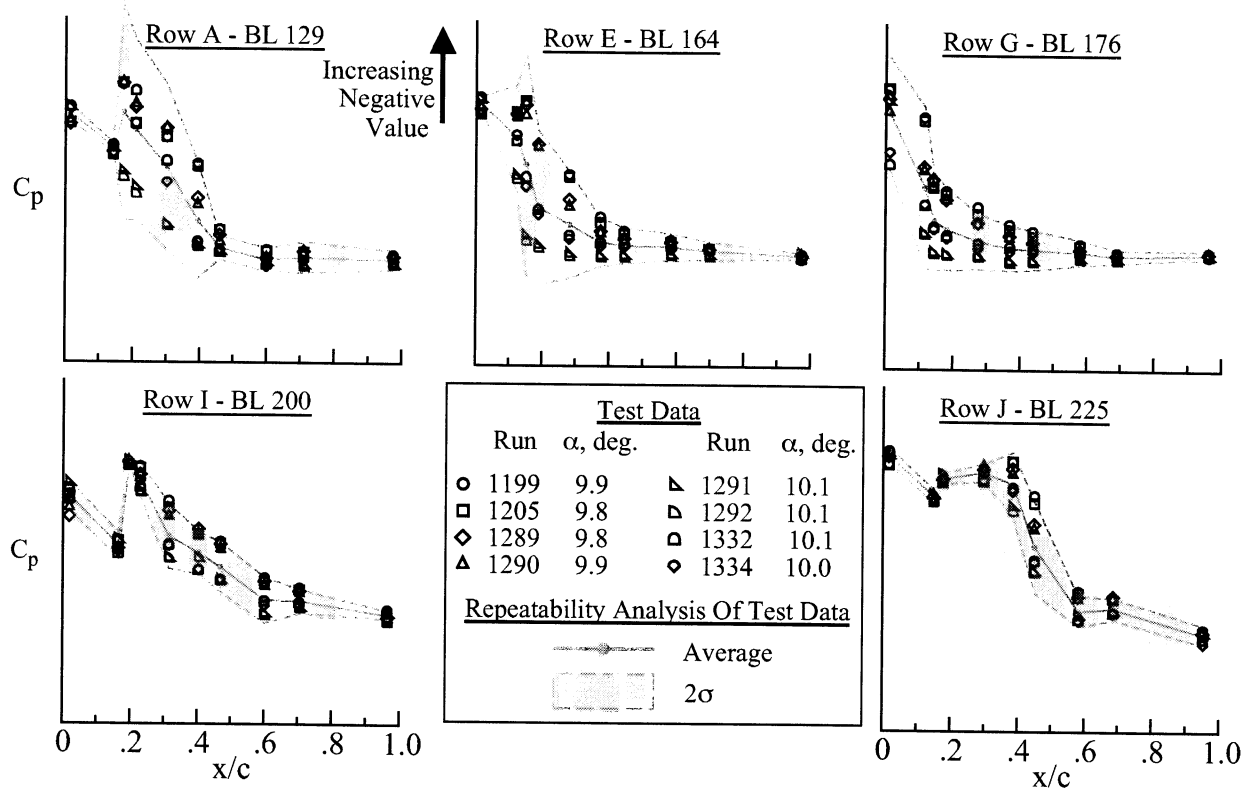

(c) $\alpha \sim 10°$.

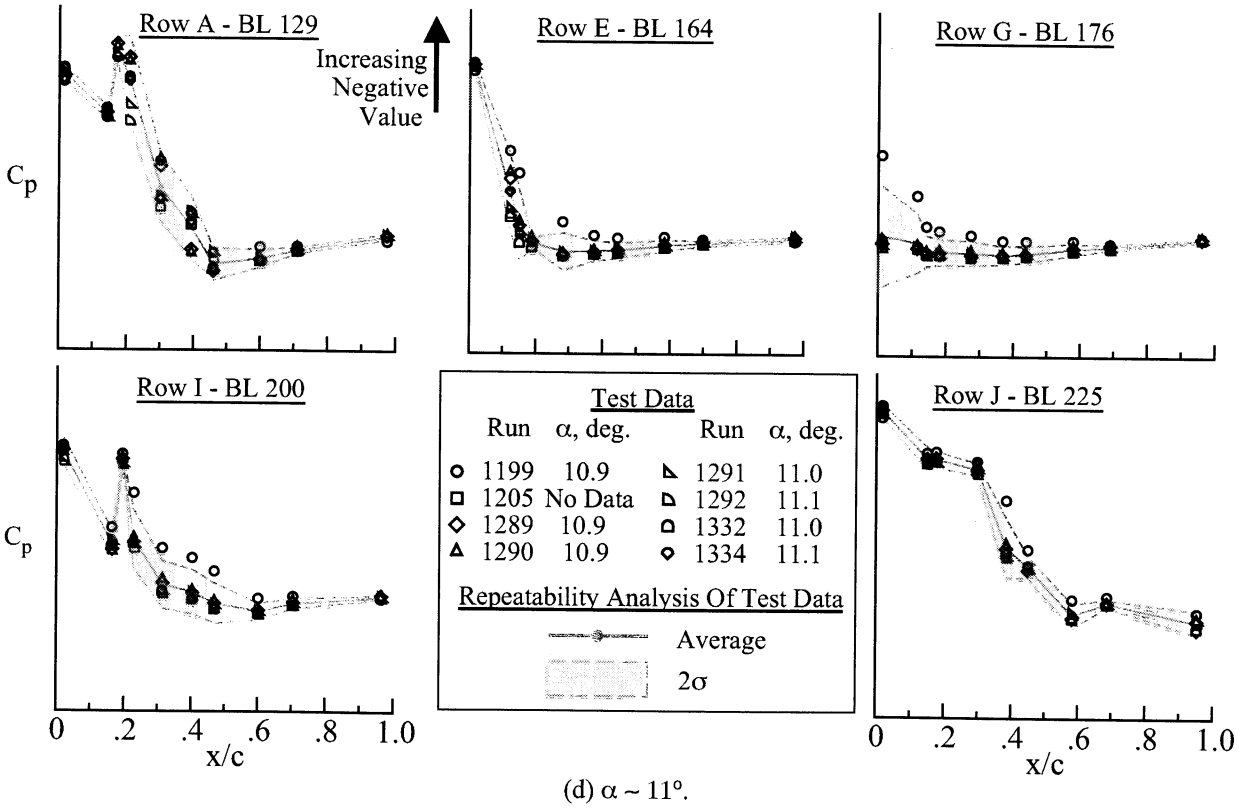

(d) $\alpha \sim 11°$.

Figure 16. Concluded.

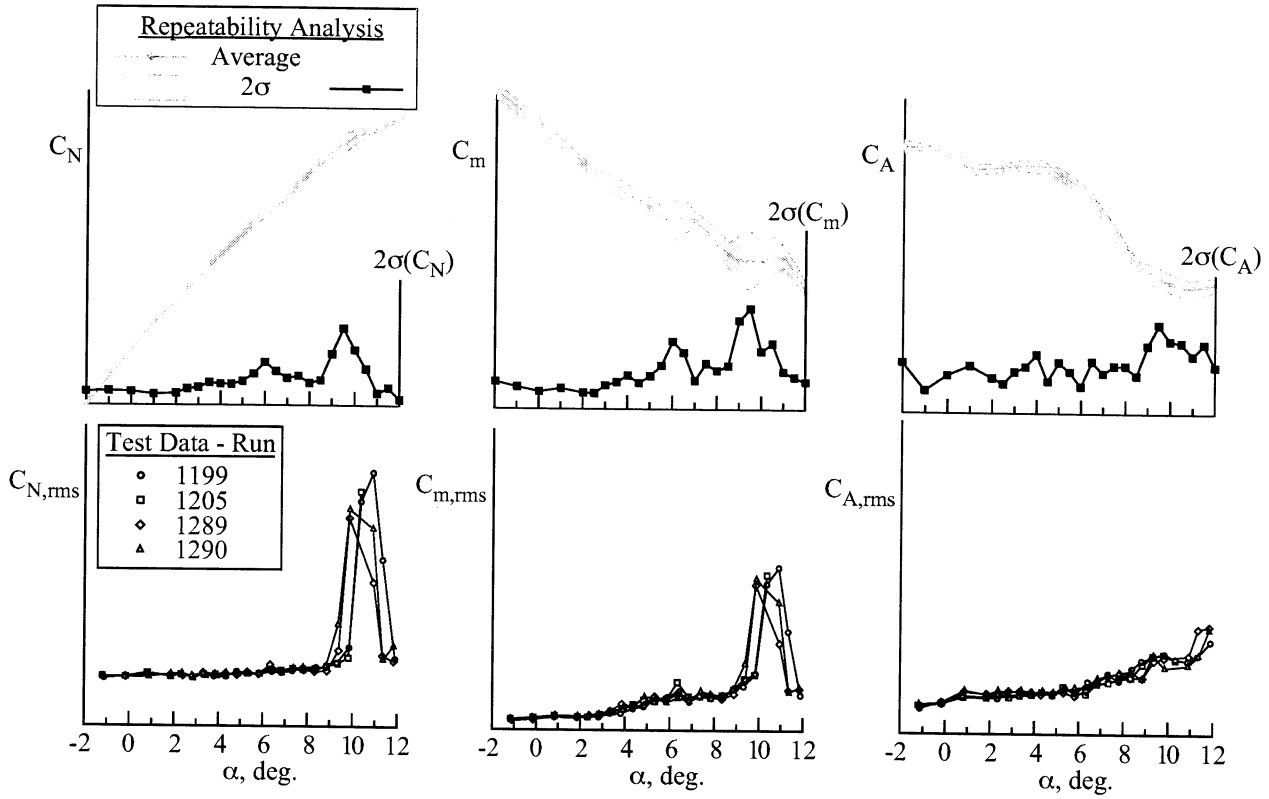

(a) C_N, C_m, and C_A data.

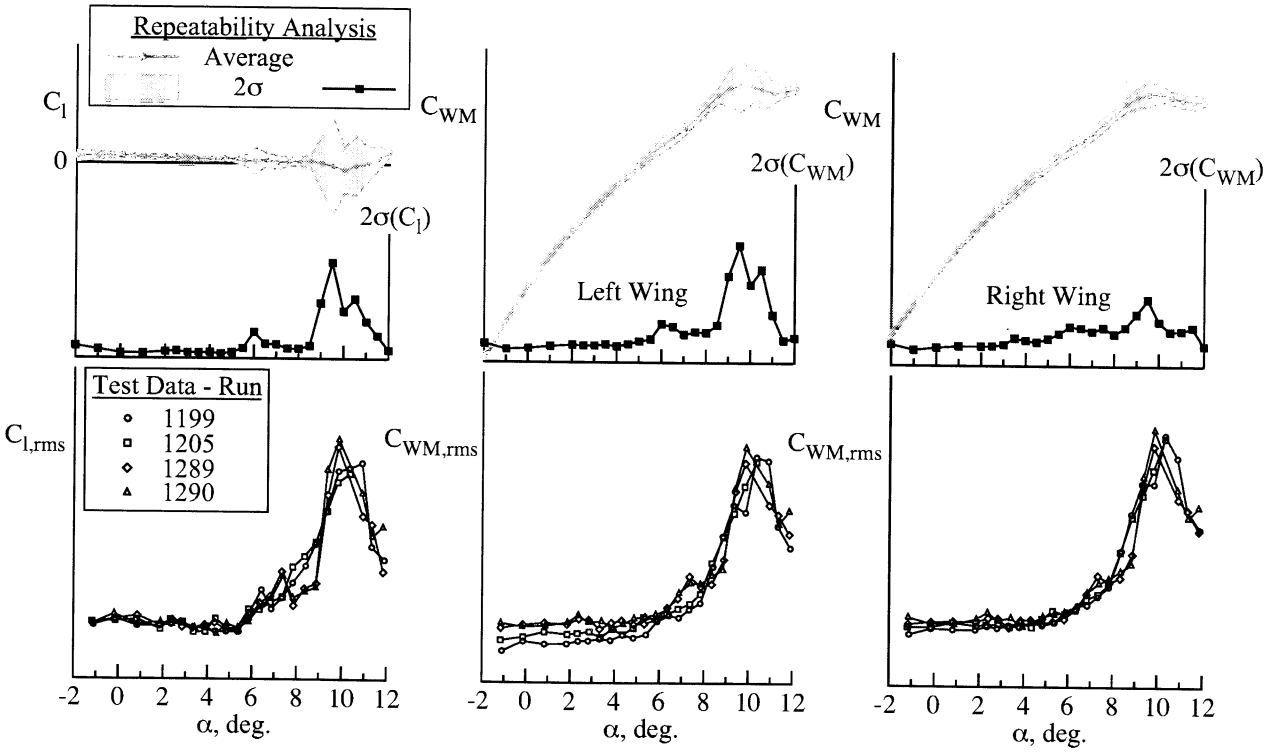

(b) C_l and C_{WM} data.

Figure 17. Comparison of repeatability analysis and measured RMS data on the baseline configuration with 10°/10°/5° flaps at M = 0.9 .

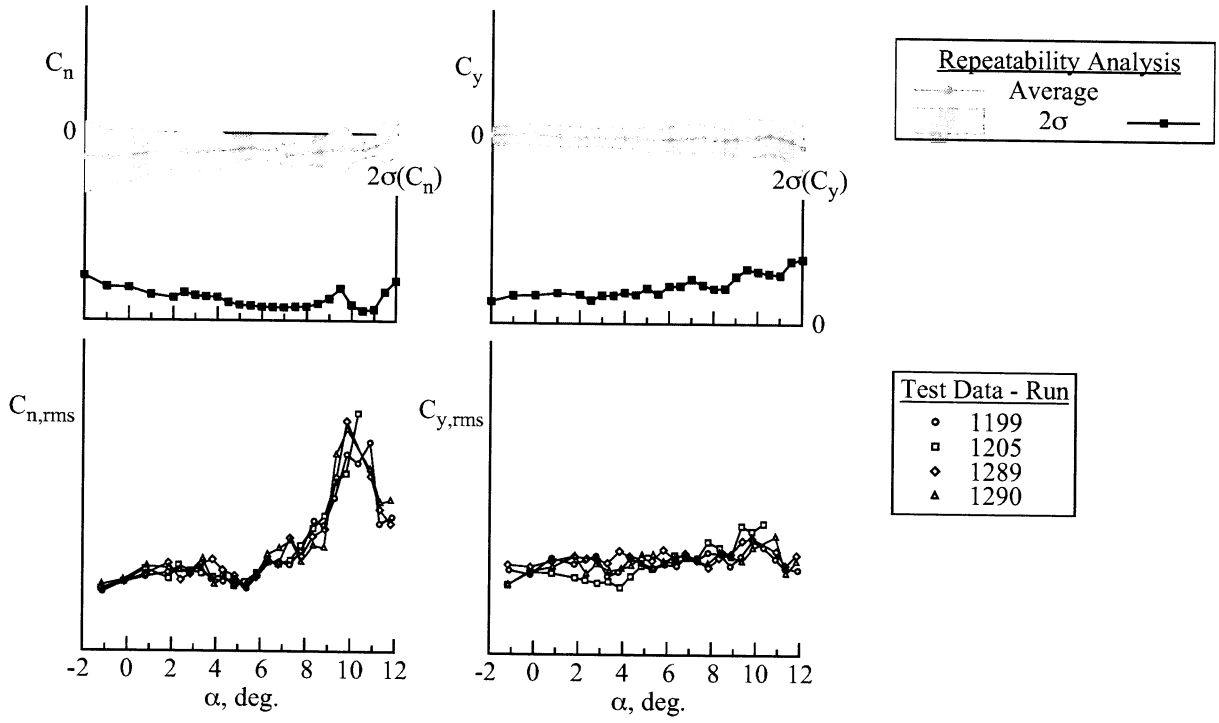

(c) C_n and C_y data.
Figure 17. Concluded.

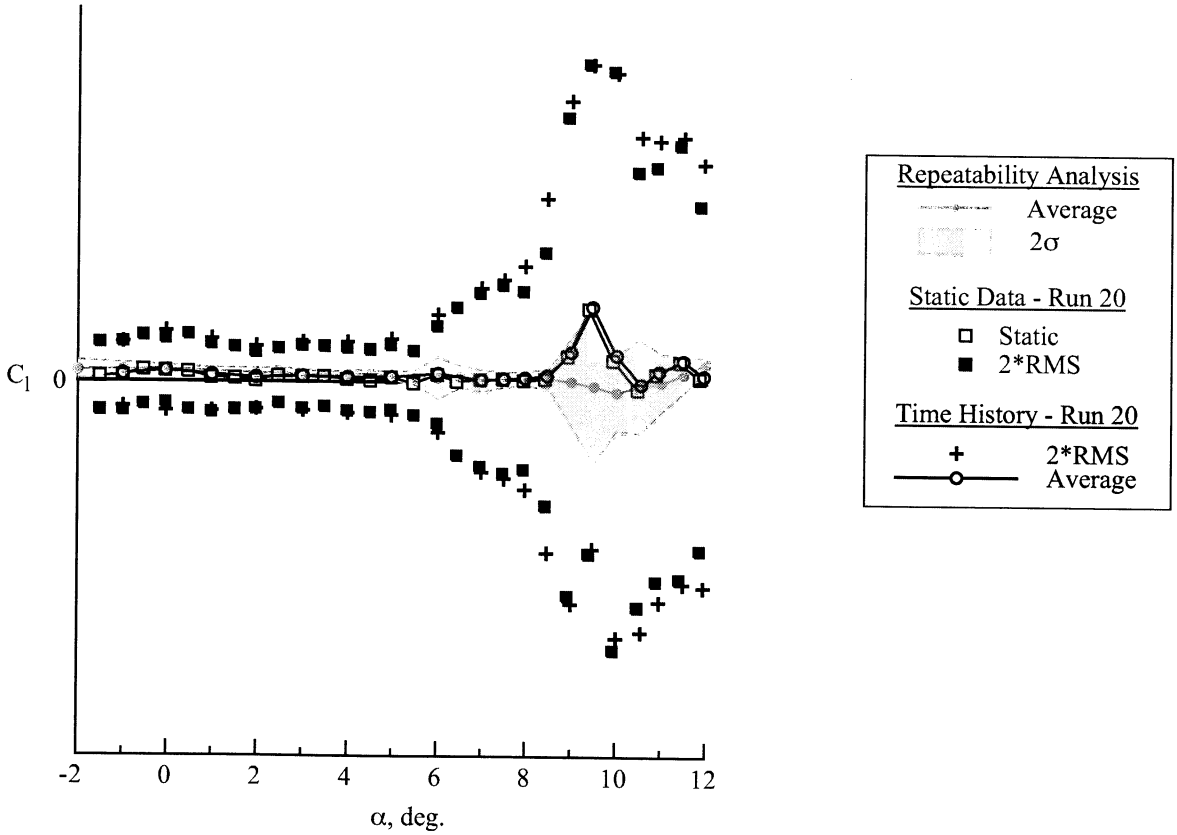

Figure 18. Comparison of repeatability analysis, static data, and time history data on the baseline configuration with 110°/10°/5° flaps at M = 0.9 .

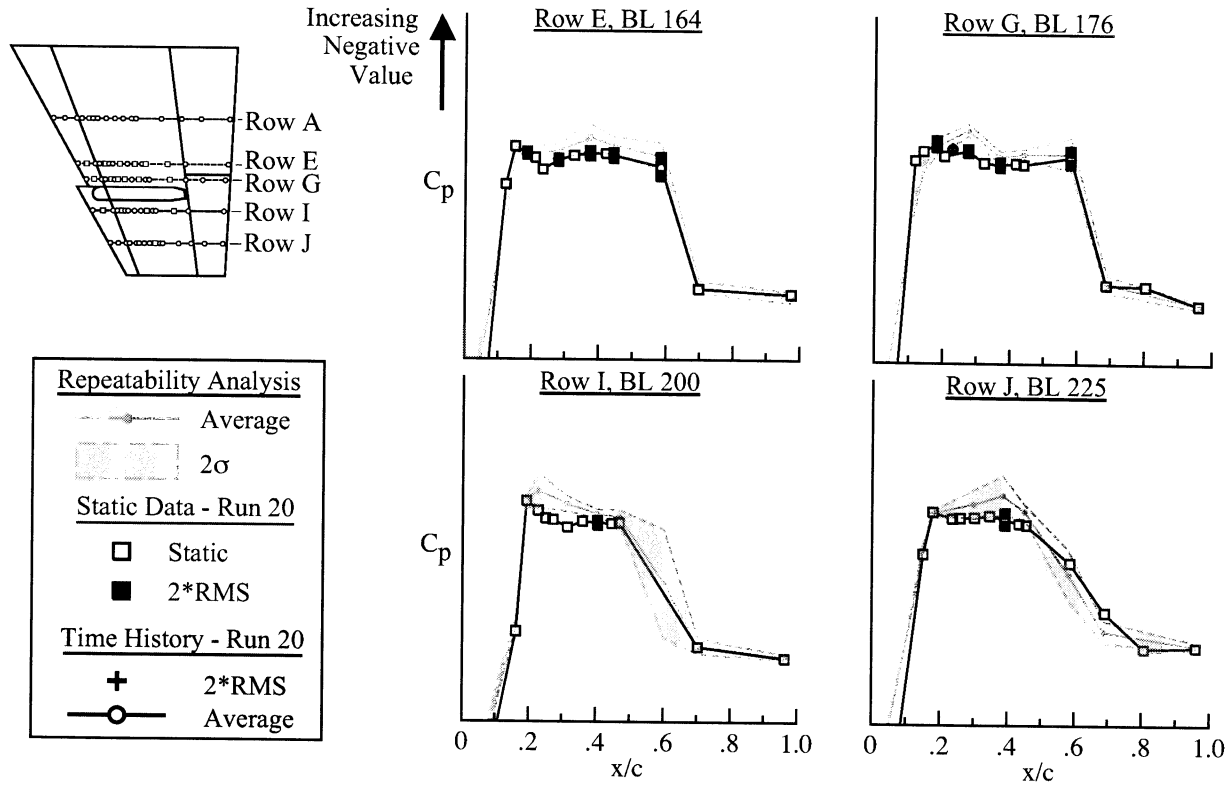

(a) $\alpha \sim 5°$.

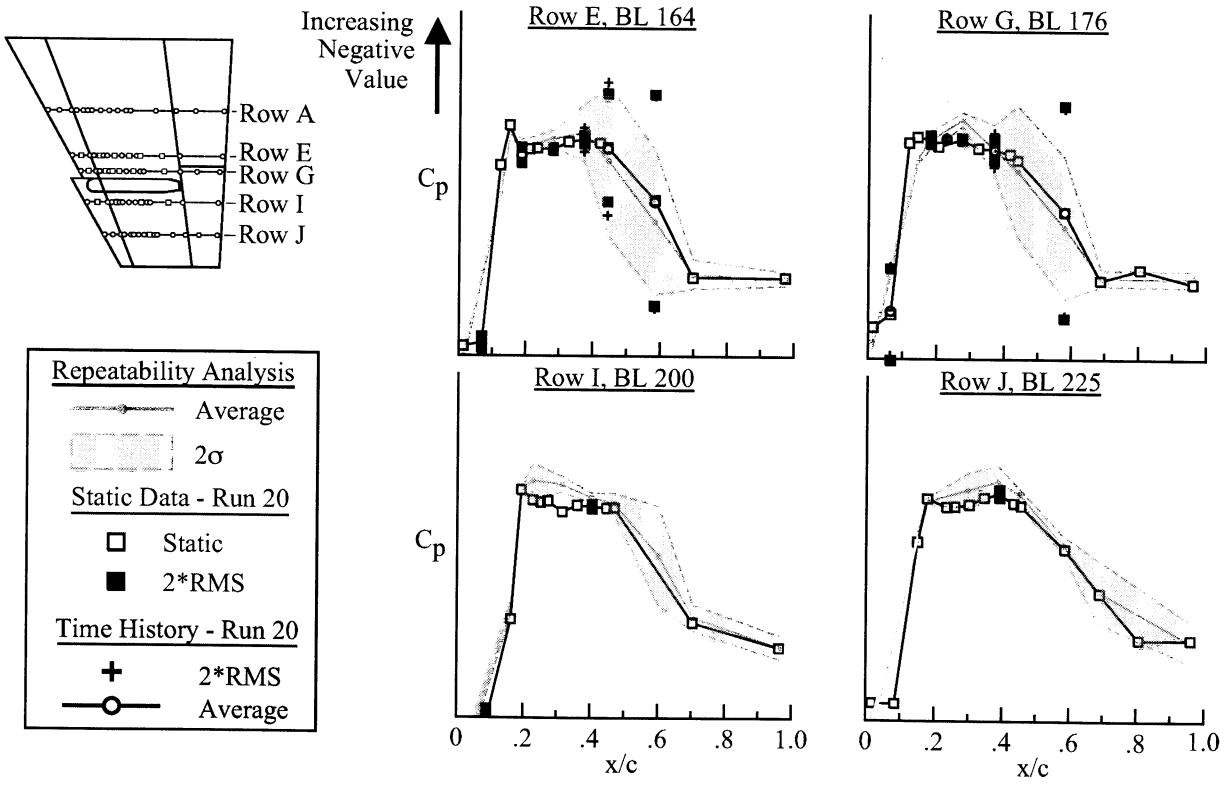

(b) $\alpha \sim 6°$.

Figure 19. Surface pressure coefficient data from the repeatability analysis, static, and time history data sets on the baseline configuration with10°/10°/5° flaps at M = 0.9 and various angles of attack.

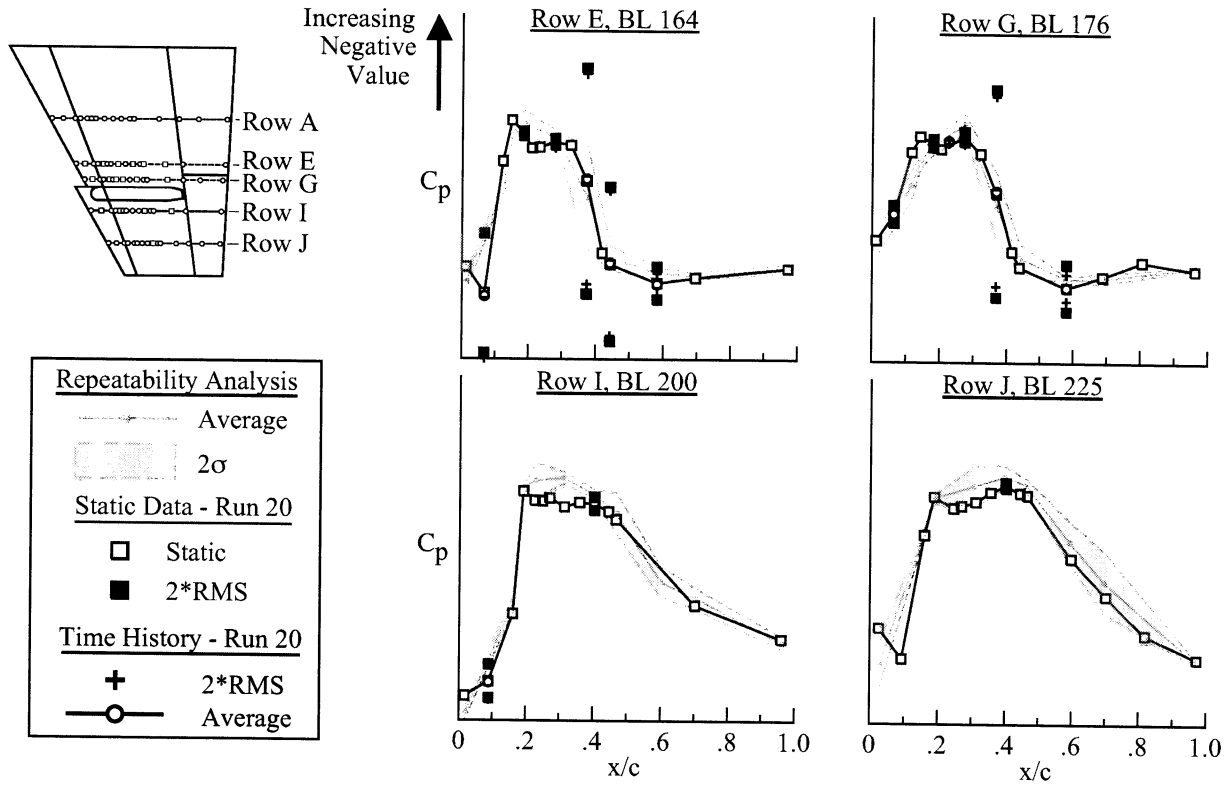

(c) $\alpha \sim 7°$.

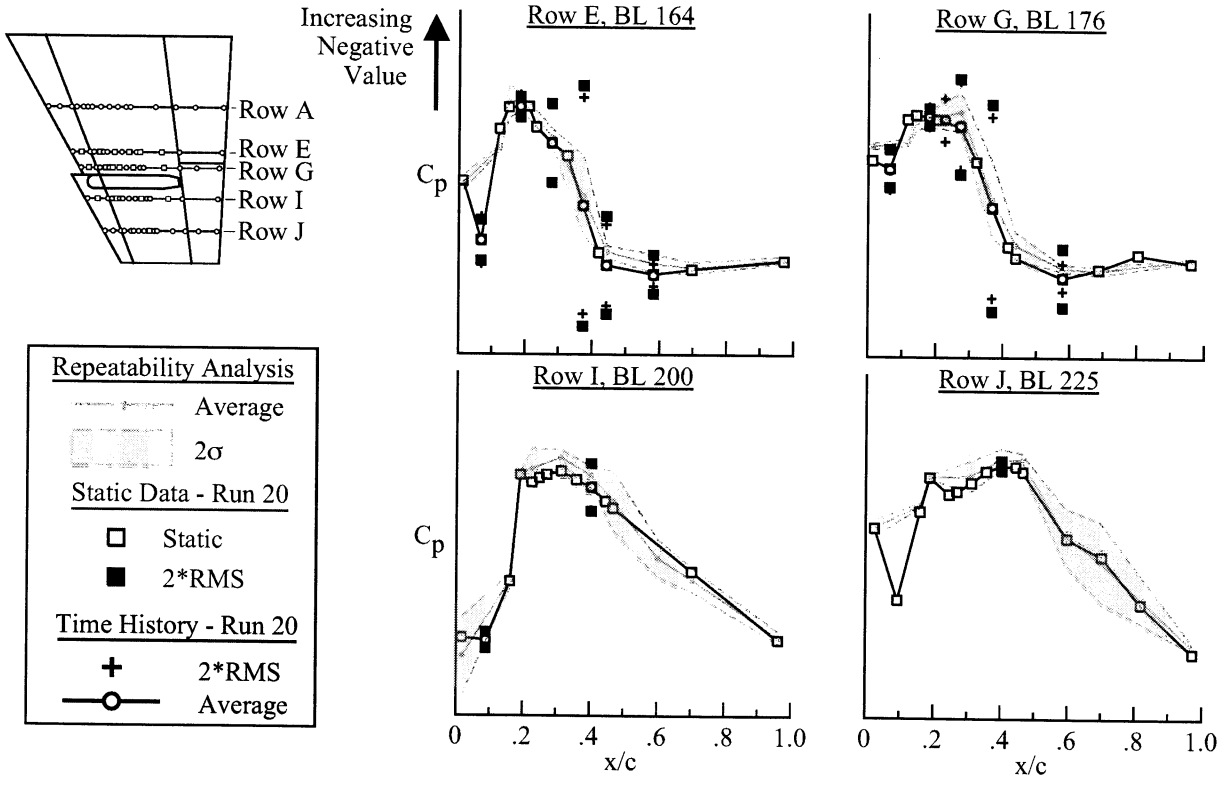

(d) $\alpha \sim 8°$.

Figure 19. Continued.

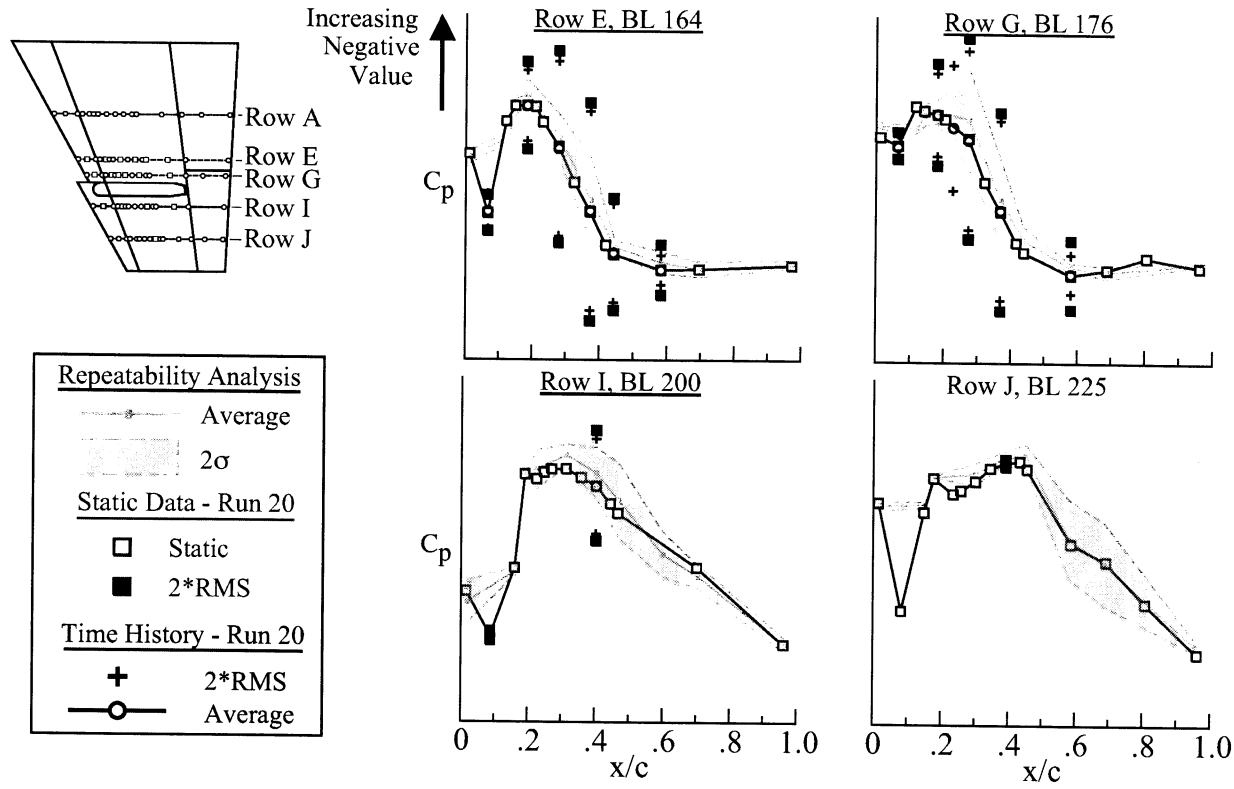

(e) $\alpha \sim 8.5°$.

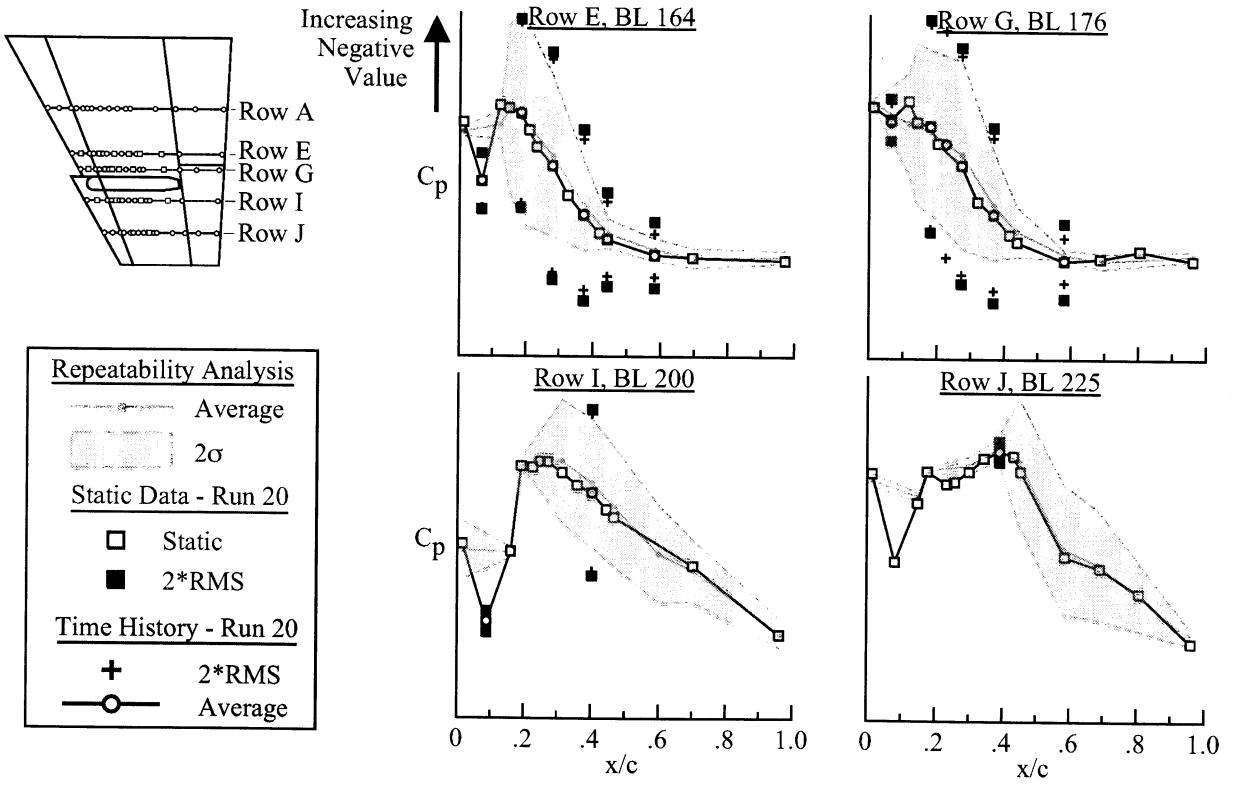

(f) $\alpha \sim 9°$.

Figure 19. Continued.

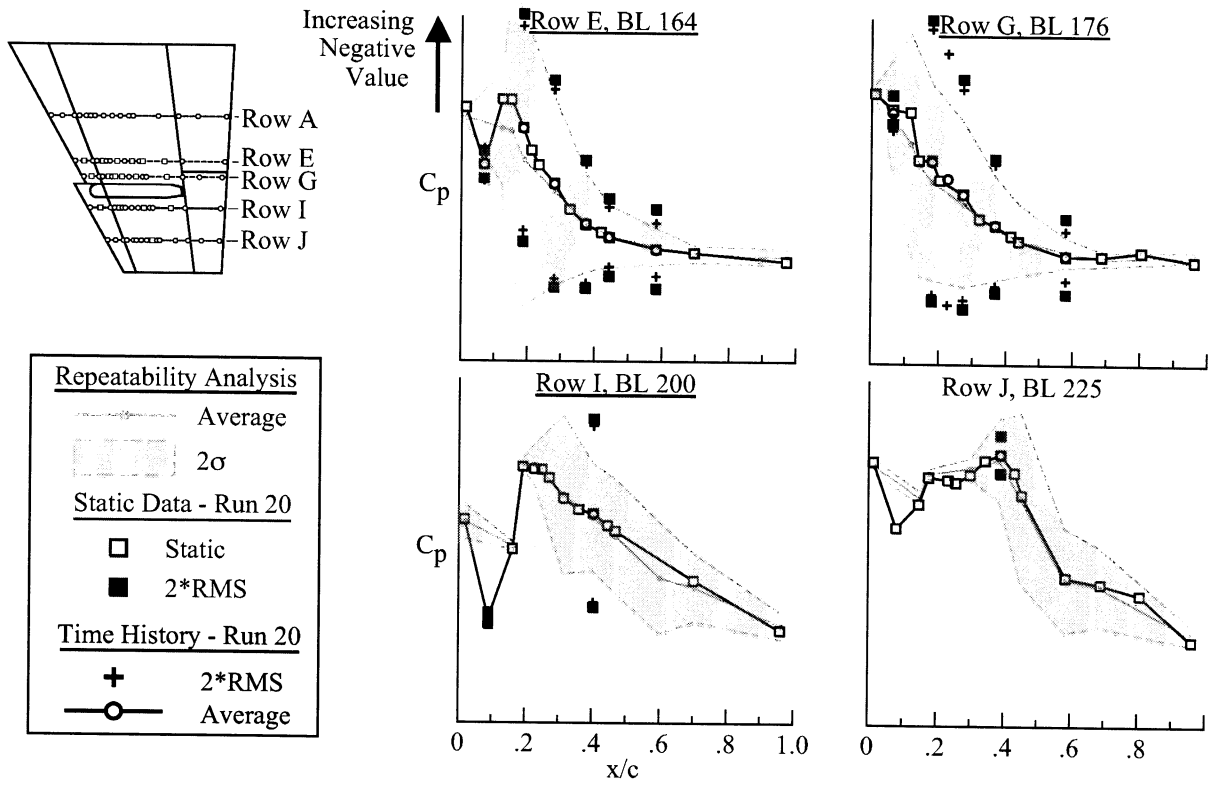

(g) $\alpha \sim 9.5°$.

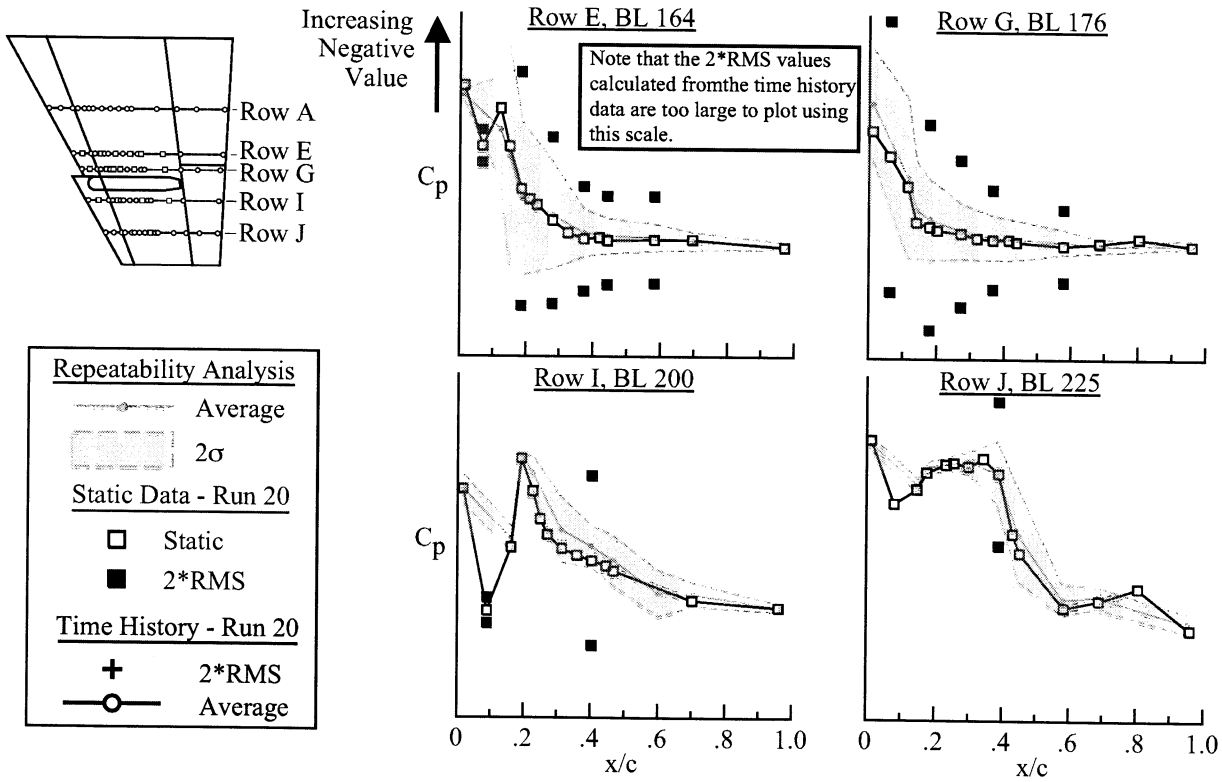

(h) $\alpha \sim 10°$.

Figure 19. Continued.

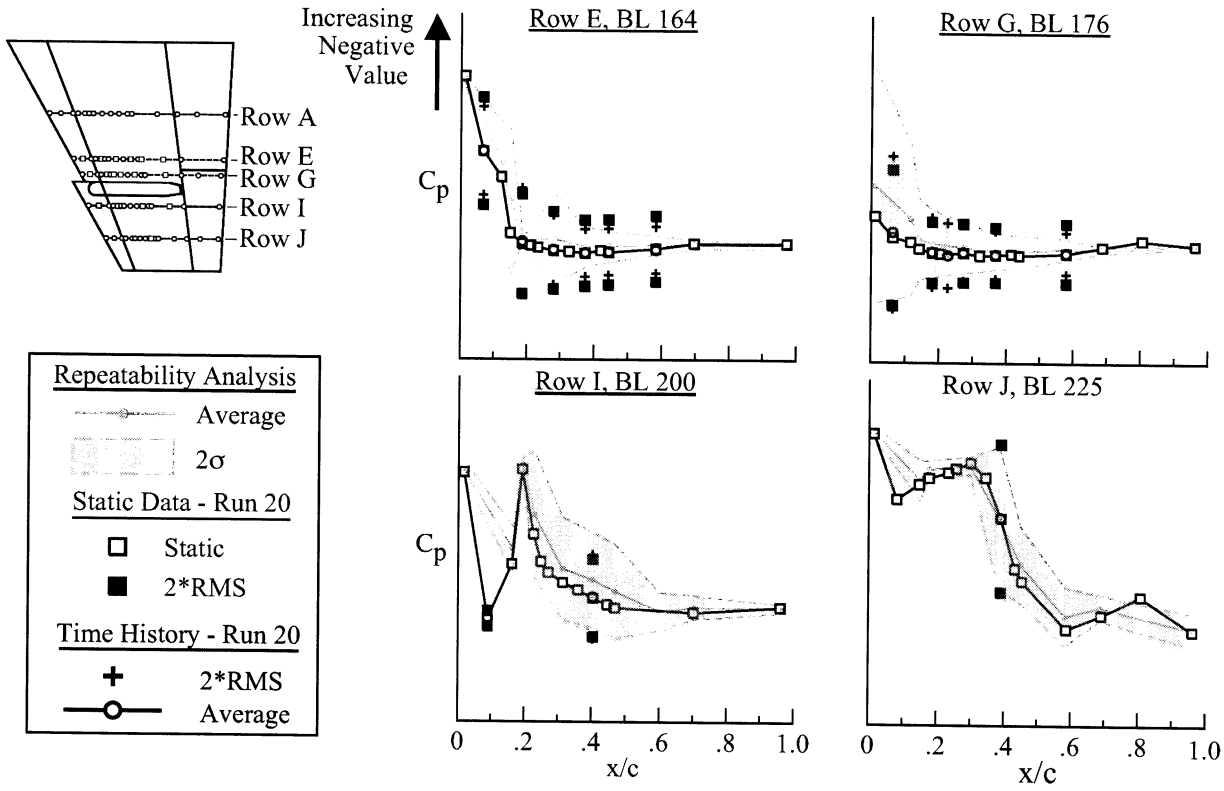

(i) $\alpha \sim 10.5°$.

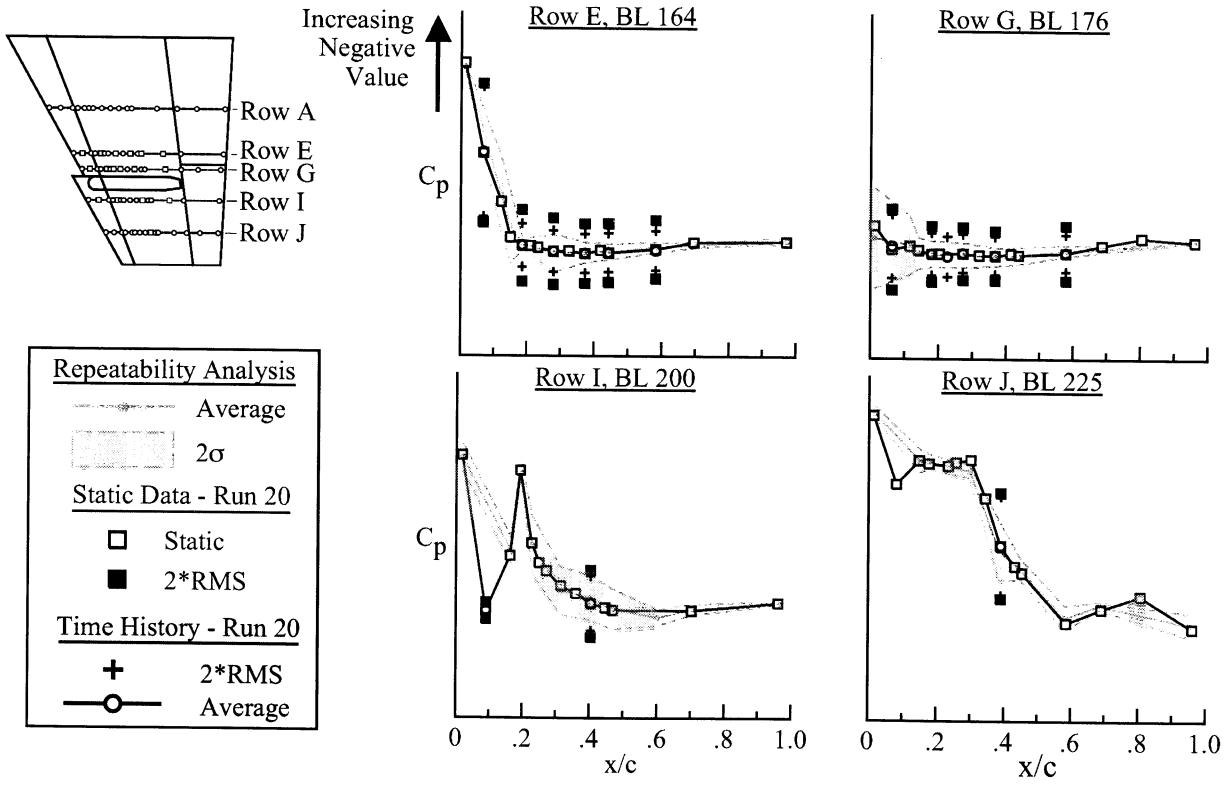

(j) $\alpha \sim 11°$.

Figure 19. Concluded.